

# Near-Infrared Spectroscopy of $0.4 < z < 1.0$ CFRS Galaxies: Oxygen Abundances, SFRs and Dust<sup>0</sup>

C. Maier<sup>1</sup>

chmaier@phys.ethz.ch

S.J. Lilly<sup>1</sup>, M. Carollo<sup>1</sup>, A. Stockton<sup>2</sup>, and M. Brodwin<sup>3</sup>

## ABSTRACT

Using new J-band VLT-ISAAC and Keck-NIRSPEC spectroscopy, we have measured  $H\alpha$  and  $[\text{N II}] \lambda 6584$  line fluxes for  $0.47 < z < 0.92$  CFRS galaxies which have  $[\text{O II}] \lambda 3727$ ,  $H\beta$  and  $[\text{O III}] \lambda 5007$  line fluxes available from optical spectroscopy, to investigate how the properties of the star forming gas in galaxies evolve with redshift. We derive the extinction and oxygen abundances for the sample using a method based on a set of ionisation parameter and oxygen abundance diagnostics, simultaneously fitting the  $[\text{O II}]$ ,  $H\beta$ ,  $[\text{O III}]$ ,  $H\alpha$ , and  $[\text{N II}]$  line fluxes. The individual reddening measurements allow us to accurately correct the  $H\alpha$ -based star formation rate (SFR) estimates for extinction. Our most salient conclusions are: a) in all 30 CFRS galaxies the source of gas ionisation is not due to AGN activity; b) we find a range of  $0 < A_V < 3$ , suggesting that it is important to determine the extinction for every single galaxy in order to reliably measure SFRs and oxygen abundances in high redshift galaxies; c) high values of  $[\text{N II}] \lambda 6584/H\alpha > 0.1$  for most (but not all) of the CFRS galaxies indicate that they lie on the high-metallicity branch of the  $R_{23}$  calibration; d) about one third of the  $0.47 < z < 0.92$  CFRS galaxies in our sample have lower metallicities than local galaxies with similar luminosities and star formation rates; e) comparison with a chemical evolution model indicates that these low metallicity galaxies are unlikely to be the progenitors of metal-poor dwarf galaxies at  $z \sim 0$ .

---

<sup>0</sup>Based on observations obtained at the ESO VLT, Paranal, Chile; ESO programs 070.B-0751, and 072.B-0496

<sup>1</sup>Department of Physics, Swiss Federal Institute of Technology (ETH Zürich), ETH Hönggerberg, CH-8093, Zürich, Switzerland

<sup>2</sup>Institute for Astronomy, University of Hawaii, 2680 Woodlawn Drive, Honolulu, HI 96822

<sup>3</sup>Jet Propulsion Laboratory, Caltech, 4800 Oak Grove Drive, Pasadena, California 91109

*Subject headings:* galaxies: abundances, galaxies: evolution, galaxies: high redshift

## 1. Introduction

The starlight that is seen at any particular redshift must be associated with the production of heavy elements which can then be seen (in stellar atmospheres or in the gas phase) at all later epochs. Monitoring how the chemical content of galaxies changes with cosmic time is thus important not only as a *per se* diagnostic of galaxy evolution, but also to constrain the history of the global star formation activity in the universe.

For many years, there have been extensive studies of the chemical composition of gas in the high redshift Universe through studies of quasar absorption line systems (see the review by Pettini et al. 2003, and references therein). More recently, there has been growing attention to measurements of the metallicities of the star-forming gas observed in distant galaxies at significant look-back times (Carollo and Lilly 2001, hereafter CL01; Hammer et al. 2001; Lilly et al. 2003, hereafter LCS03; Kobulnicky et al. 2003; Maier et al. 2004; Mehlert et al. 2002; Pettini et al. 2002). In the main, these measurements have focussed on the oxygen abundance,  $[O/H]$ , as computed from a number of empirically calibrated metallicity estimators based on the relative strengths of strong emission lines. The most popular of these estimators has been the  $R_{23}$  parameter introduced by Pagel et al. (1979), which is defined as  $R_{23} = ([O II] \lambda 3727 + [O III] \lambda\lambda 4959, 5007)/H\beta$ .

A main reason for the success of  $R_{23}$  as a gas metallicity estimator at intermediate redshifts is that it is relatively easy to measure, as the observed wavelengths of the  $[O II] \lambda 3727$ ,  $[O III] \lambda\lambda 4959, 5007$  and  $H\beta$  lines remain, at  $z < 1$ , in the optical window. Indeed, the use of  $R_{23}$  has provided key information, albeit coarse, on the gas metallicities of several dozens of intermediate redshift galaxies, and thus opened the possibility of investigating, in a statistically meaningful way, the chemical evolution with cosmic time of the normal galaxy population. Specifically, after initial results for a subsample of 15 galaxies were published in CL01, LCS03 provided gas oxygen abundances based on  $R_{23}$  for a total sample of 66  $0.47 < z < 0.92$  CFRS galaxies.

There are however some limitations in all work based on the  $R_{23}$  estimates. First, it is well known that  $R_{23}$  is degenerate with metallicity, as low  $R_{23}$  values can be associated with either high or very low  $[O/H]$  values. Furthermore,  $R_{23}$  is significantly affected by dust extinction. In CL01 and LCS03 it was *assumed* that the CFRS galaxies lie on the

high-metallicity branch of the  $R_{23}$ -metallicity relation, and the spectra were dereddened assuming a uniform  $E_{B-V} = 0.3 \pm 0.15$ , i.e., the average for galaxies of the Nearby Field Galaxy Sample (Jansen et al. 2000). Eliminating these sources of potential error requires a determination of the reddening as well as breaking the  $R_{23}$  degeneracy, for each galaxy individually. This can be achieved with knowledge of the  $H\alpha$  and  $[\text{N II}] \lambda 6584$  lines fluxes, which, at intermediate redshifts, are shifted into the near-infrared (NIR) wavelength window. Specifically, the reddening by dust can be estimated by means of Balmer lines ratios, e.g., the  $H\alpha/H\beta$  ratio, and the degeneracy in  $R_{23}$  can be broken by measuring the  $\text{NII}/H\alpha$  ratio.

In this paper we present new measurements of  $H\alpha$  and  $[\text{N II}] \lambda 6584$  for 28 of the  $0.47 < z < 0.92$  CFRS galaxies investigated in LCS03 supplemented by CFHT optical spectra to derive  $H\alpha$  and  $[\text{N II}] \lambda 6584$  for two galaxies at  $z = 0.472$  and  $z = 0.479$ . We use these new measurements to derive accurate estimates for the gas oxygen abundance, dust extinction and star formation rate (SFR) in the sample galaxies. The paper is structured as follows: In Sect. 2 we describe the new near infrared data, acquired with VLT/ISAAC and Keck/NIRSPEC, and the data reduction procedure. In Sect. 3 we describe the derivation of the oxygen abundances. These were obtained through a simultaneous fit of the  $[\text{O II}] \lambda 3727$ ,  $H\beta$ ,  $[\text{O III}] \lambda 5007$ ,  $H\alpha$ , and  $[\text{N II}] \lambda 6584$  lines in terms of extinction parameter  $A_V$ , ionisation parameter  $q$ , and  $[\text{O}/\text{H}]$ , using the set of ionisation parameter and oxygen abundances developed by Kewley & Dopita (2002, hereafter KD02). This procedure provides metallicity estimates which should be more robust than those obtained from individual line ratios (as done, e.g., by Kobulnicky et al. (2003), Kobulnicky & Kewley (2004), Shapley et al. (2004), and in our own CL01 and LCS03). In Sect. 4 we present the results of our analysis, i.e., the extinction, SFRs, and oxygen abundances of the 30 CFRS galaxies. We then compare these measurements with the properties of galaxies in the local universe, and discuss a scenario for the chemical evolution of galaxies at  $0 < z < 1$ . Finally, in Sect. 5 we present our conclusions.

A “concordance” cosmology with  $H_0 = 70 \text{ km s}^{-1} \text{ Mpc}^{-1}$ ,  $\Omega_0 = 0.3$ ,  $\Omega_\Lambda = 0.7$  is used throughout this paper. Note that, unless otherwise specified, the terms *metallicity* and *abundance* are used to indicate *oxygen abundance* of the line emitting gas throughout this paper.

## 2. Near-infrared observations, data reduction, and line flux measurements

The 30  $0.47 < z < 0.92$  CFRS galaxies investigated in this paper are extracted from the 66 objects sample presented in LCS03. They form an essentially random sub-sample. All the galaxies have therefore  $[\text{O III}] \lambda 5007$ ,  $H\beta$ , and  $[\text{O II}] \lambda 3727$  lines measured with the

CFHT. The galaxies have absolute B magnitudes  $M_{B,AB} < -19.5$ .

For two objects at  $z = 0.472$  and  $z = 0.479$ ,  $H\alpha$  and  $[N II] \lambda 6584$  measurements could already be obtained from the optical CFHT spectra presented in LCS03. For the remaining 28 galaxies discussed in this paper, new  $H\alpha$  and  $[N II] \lambda 6584$  measurements were obtained from VLT and Keck NIR spectroscopy. For easy reference, we report in Table 1 the photometry, line fluxes (including the new  $H\alpha$  and  $[N II] \lambda 6584$ ), and other information we have collected for the 30 CFRS galaxies.

## 2.1. The VLT-ISAAC spectra

Near-infrared spectroscopy for 17  $0.5 < z < 0.92$  CFRS galaxies of LCS03 was obtained with the ISAAC spectrograph at the VLT in order to measure their  $H\alpha$  and  $[N II] \lambda 6584$  line fluxes. The observations were carried out in October 2002 (Program 070.B-0751A, hereafter P70), and November/December 2003 plus September/October 2004 (Program 072.B-0496A, hereafter P72). The medium resolution grism was used with the Short-Wavelength channel equipped with a  $1024 \times 1024$  pixel Hawaii array. The pixel scale is  $0.147''$  per pixel. We used a slit of  $2''$  width, which results in a nominal resolution of  $R \sim 1500$ .

We used two different filters, i.e., the SZ and the J filter, in order to select the 5th and 4th grating order for measuring the  $H\alpha$  and  $[N II] \lambda 6584$  lines of galaxies at  $0.5 < z < 0.65$  and  $0.7 < z < 0.92$ , respectively. The covered wavelength range was 59 nm and 46 nm when using the J and the SZ filter, respectively. The corresponding pixel scales were  $0.58\text{\AA}/\text{pixel}$  and  $0.45\text{\AA}/\text{pixel}$ .

The individual integration times varied between 1200 s and 4800 s. During the observations the telescope was nodded between two positions  $\sim 10''$  apart along the slit in P70, and between eight positions  $\sim 5''$  apart in P72. Dark frames, flat-fields and (Xe+Ar) arc lamp spectra were taken with the same filter, central wavelength and slit width for each of the targets observed during the night. The conditions were photometric during these observations (see Table 2 for further details).

### 2.1.1. Processing of the 2D galaxy spectra

$1024 \times 800$  pixel frames were extracted from the original  $1024 \times 1024$  pixel raw frames. A flat field was obtained by normalizing the difference between a lamp-on and a lamp-off image. The individual science frames were subtracted of dark, and flat-fielded. Cosmic rays were removed in every single exposure using the IRAF routine *cosmicrays*. Wavelength cal-

ibration and a geometrical distortion correction were performed using arc spectra of xenon and argon. A 3rd order Legendre polynomial provided an adequate fit to the dispersion relation. Typical relative uncertainties of the dispersion relation were of order  $\sim 1/10$  of a pixel, corresponding to  $\sim 0.06\text{\AA}$ . The background was determined by applying the IRAF procedure *median* to each individual 2D spectra using a sliding rectangular window of dimension  $1 \times 201$  pixels in the x and y direction, respectively. This background was subtracted from each science frame.

For each galaxy, a median sky was obtained by masking out the galaxy spectrum in each of the (two or eight for P70 and P72, respectively) individual dithered frames, and applying a median algorithm to the stack of masked frames. The median sky was then subtracted from each individual dithered image. The final 2D spectrum was obtained by aligning and averaging these sky-subtracted frames.

### 2.1.2. Spectrophotometric calibration

Calibration of spectroscopic data in the NIR is simplified by the use of stars hotter than B4. These have relatively featureless spectra and allow one to correct the telluric features of the Earth’s Atmosphere and to calibrate fluxes in the NIR wavelength window. We used six telluric standards from the Hipparcos catalogue to calibrate our VLT spectra (see Table 2). The six stars were observed under photometric conditions. These stars have measured V band magnitudes, V-I colours, spectral types, and JHK band magnitudes. This leads to uncertainties of about 10% in the absolute flux calibration.

After bias subtraction, flat fielding, wavelength calibration and geometric distortion correction using IRAF routines, the standards 1D spectra were extracted from the resulting 2D frames, the sensitivity response as a function of wavelength was determined using a 3rd order Legendre function, and the the flux calibration was done, after correcting the spectra for (small) air-mass effects.

### 2.1.3. Extraction of the one-dimensional galaxy spectra

The one-dimensional spectra of each galaxy were extracted using the algorithm by Horne (1986) with an aperture of 10-15 pixels in y-direction, i.e. about  $1.5-2''$ . An effective spectral resolution element of  $\text{FWHM} \sim 8\text{\AA}$  in the J filter, and  $\text{FWHM} \sim 5.9\text{\AA}$  in the SZ filter, i.e., 13-14 pixels, was estimated from the calibration lines. We therefore smoothed the reduced 1D spectra when displaying them in Figs. 1 and 2, to sample the spectral resolution element,

thereby maximizing the S/N ratio without any loss of information. A Gaussian filter was used as a kernel for the smoothing, as a Gaussian shape well reproduces the typical instrumental profile and thus minimizes any change of shape in the profiles of the observed spectra lines.

## 2.2. The Keck—NIRSPEC Spectra

Eleven galaxies were observed using NIRSPEC at Keck II on the nights of June 14/15 2000, 29/30 March 2004, and 30/31 March 2004. NIRSPEC was designed primarily as a high-dispersion echelle spectrograph. We used it in the low-dispersion mode, which replaces the echelle with a mirror, so that the dispersion is provided by the order-sorting grating. The resulting spectrum is tilted by about  $6^\circ$  from the orientation of the  $1024 \times 1024$  Alladin array columns, and the dispersion varies slightly along the projected slit.

The objects were moved on the slit in an A-B-B-A pattern for each 4-exposure sequence, each exposure being 600 s. For each exposure, the following steps were taken before correcting for distortion, in order to optimize both the airglow subtraction and the removal of cosmic rays. For, say, the first exposure at the “A” position, the two exposures at the “B” position were averaged, Gaussian smoothed slightly parallel to the airglow lines to minimize added noise, scaled to match as closely as possible the airglow lines in the region of redshifted  $H\alpha$ , and subtracted. We used the *lacos\_im* task (van Dokkum 2001) to remove cosmic rays. We then added back the subtracted spectrum. The resulting spectrum is simply the original spectrum with cosmic rays removed.

After this procedure was carried out for each of the 4 spectra of a group, we repeated the process, using the cosmic-ray-free spectra and retaining the difference image, which was now free of cosmic rays (including the negative cosmic-ray residuals from the original subtraction) and largely free of airglow lines, although some slight positive and negative residuals remained.

At this point, we rectified the spectrum, corrected for distortion, and applied the wavelength calibration (derived from the airglow lines), using the *wmkonspec* IRAF package. Airglow residuals were removed from the rectified spectra by fitting a cubic spline (with outlier rejection) to each row (i.e., the cross-dispersion dimension) and subtracting. The 1-D spectra were extracted from these images, some additional manual cleaning of “unfeasible noise” was done, and the final spectra were averaged together.

Final calibration and correction for telluric absorption was carried out with the aid of observations of the A0 V stars HD 89239 and 86 UMa, and the A2 star HD 129653. The procedures were similar to those described in Section 2.1.2, the main difference being the

need to interpolate across the Pa- $\beta$  or Pa- $\gamma$  lines in the standards in some cases. The 1D flux calibrated spectra from Keck are shown in Fig. 3.

### 2.3. Measurement of the H $\alpha$ and [N II] $\lambda$ 6584 fluxes, and line ratios

The H $\alpha$  and [N II]  $\lambda$  6584 fluxes (see Table 1) were measured using the package *splot* in IRAF. The flux errors were usually dominated by systematic uncertainties in establishing the local continuum. The latter was conservatively estimated by exploring rather extreme possibilities. As in LCS03, we assumed that the flux of [O III]  $\lambda$  4959 is 0.34 of the flux of [O III]  $\lambda$  5007. Similarly, we assumed an average underlying stellar absorption in H $\beta$  of  $3 \pm 2 \text{ \AA}$  and corrected the equivalent width of this line by this, thereby increasing the H $\beta$  line flux. The treatment of Balmer absorption propagates through to  $A_V$ , e.g., correcting too much for the H $\beta$  absorption would lead to an underestimate of the reddening and vice versa. Using  $3 \pm 2 \text{ \AA}$  to correct the H $\beta$  absorption, the error bars should reflect this uncertainty. We have not applied any correction to the H $\alpha$  line which has an observed equivalent width larger than  $50 \text{ \AA}$  for all 30 CFRS galaxies (see Table 1).

A key issue for the measurement of extinction is the matching between the near-infrared and optical spectra. We used comparable slits for the optical and the near-infrared spectroscopy, and in the good seeing conditions encountered the resulting emission line fluxes from the spectroscopy should approximate “total” fluxes. To check the accuracy of the relative calibration between H $\alpha$  measurements and the H $\beta$  fluxes measured with CFHT, we compared, for the seven objects with a detectable continuum, the value of the continuum at the position of H $\alpha$  with the continuum at H $\beta$ . These two measurements of the continuum were found to be consistent at the 10% level with the broad band magnitudes of the target galaxies.

## 3. Our method to determine gas oxygen abundances

Our approach to determine gas oxygen abundances is based on the models of KD02, who developed a set of ionisation parameter and oxygen abundance diagnostics based on the use of only strong optical emission lines. The method consists in performing a simultaneous fit to the [O II]  $\lambda$  3727, H $\beta$ , [O III]  $\lambda$  5007, H $\alpha$ , and [N II]  $\lambda$  6584 lines in terms of extinction parameter  $A_V$ , ionisation parameter  $q$ , and [O/H].

For each set of metallicities, KD02 give third order polynomial fits to the relation between [O III]  $\lambda$  5007/[O II]  $\lambda$  3727 and the ionisation parameter  $q$ . These have the form:

$$\log([\text{OIII}]/[\text{OII}]) = k_0 + k_1 \log q + k_2 (\log q)^2 + k_3 (\log q)^3 \quad (1)$$

where  $k_{0-3}$  are constants given in Table 2 of KD02.

For each ionisation parameter, fourth order polynomials are used to fit the model curves relating the flux ratios (or  $R_{23}$ ) and metallicity:

$$\log(R) = k'_0 + k'_1 x + k'_2 x^2 + k'_3 x^3 + k'_4 x^4 \quad (2)$$

where  $R$  is either  $[\text{NII}]/\text{H}\alpha$ , or  $R_{23}$ ,  $k'_{0-4}$  are constants given in Table 3 of KD02, and the variable  $x$  is the metallicity,  $12 + \log(\text{O}/\text{H})$ .

Using these relations between  $[\text{O III}] \lambda 5007/[\text{O II}] \lambda 3727$ ,  $[\text{N II}] \lambda 6584/\text{H}\alpha$ , and  $R_{23}$ , and the relations between  $[\text{O}/\text{H}]$ ,  $A_V$ , and  $q$ , we created a model grid of relative line strengths as a function of three parameters: the extinction parameter,  $A_V$ , the ionisation parameter,  $q$ , and the oxygen abundance,  $12 + \log(\text{O}/\text{H})$ . The ranges for the values of the parameters, and the details of the adopted grid are given in Table 3. The grid contains a total of  $\sim 12 \times 10^6$  models and is described in detail in the next section.

It should be noted that there might be systematic uncertainties in the KD02 models, but our philosophy is to treat all galaxies at high and low redshift in the same way. Starting with the observed line fluxes (ratios) and computing oxygen abundances with the same method for the low and high redshift galaxies (as also suggested and as very important seen by Salzer et al. 2005) will allow us to focus on relative effects between the selected samples in the expectation that these are likely to be much more robust than attempts to determine very accurately the absolute metallicity.

### 3.1. Extinction and model line fluxes $M_i$

The dereddened value for a flux line ratio,  $I(\lambda_1)/I(\lambda_2)$ , is given by:

$$\frac{I(\lambda_1)}{I(\lambda_2)} = \frac{F(\lambda_1)}{F(\lambda_2)} \times 10^{c(f(\lambda_1)-f(\lambda_2))}, \quad (3)$$

where  $F(\lambda)$  is the observed flux at a given wavelength,  $c$  is the logarithmic reddening parameter that describes the amount of reddening relative to  $\text{H}\beta$ , and  $f(\lambda)$  is the wavelength-dependent reddening function (Whitford 1958).  $f(\lambda)$  can be approximated in the whole spectral range to an accuracy better than 5% with the expression  $f(\lambda) = 3.15854 \times 10^{-1.02109\lambda} - 1$ , where  $\lambda$  is in units of  $\mu\text{m}$ , see Izotov et al. (1994). The value of  $c$  can be estimated from the

relation  $c = 1.47 \times E_{B-V} = 1.47 \times A_V/3.2$ , and the dereddened flux of an observed emission line is  $F_{der} = F_{obs} \times 10^{c(1+f(\lambda))}$  (Seaton 1979).

The  $H\alpha/H\beta$  line ratio is quite insensitive to the assumed density and not very sensitive to the electron temperature, see Table 4.4 in Osterbrock (1989). Assuming case B Balmer recombination, with a temperature of 10 000 K, and a density of  $100 \text{ cm}^{-3}$  (Brocklehurst 1971), the predicted dereddened intensity ratio of  $H\alpha$  to  $H\beta$  is 2.86 (Osterbrock 1989). The effect of reddening on the ratio  $H\alpha/H\beta$  can be written as  $I(H\alpha)/I(H\beta) = F(H\alpha)/F(H\beta) \times 10^{(-0.332)c}$ .

We normalized the model fluxes relative to  $H\alpha$ , i.e., the  $H\alpha$  flux was set to one, and the correction for extinction assuming case B recombination was calculated relative to  $H\alpha$ . The dust reddened model value for  $H\beta$  (to be compared with the observed dust reddened emission line flux) is thus calculated according to:

$$F(H\beta) = \frac{F(H\alpha)}{2.86} \times 10^{-0.332c}. \quad (4)$$

To get the model value for the  $[N II] \lambda 6584$  flux,  $[N II] \lambda 6584/H\alpha$  is calculated using equation 2, and then:

$$F([N II] \lambda 6584) = \frac{F([N II] \lambda 6584)}{F(H\alpha)} \times 10^{0.003c}. \quad (5)$$

To calculate the model value for the  $[O II] \lambda 3727$  flux, first  $[O III] \lambda 5007/[O II] \lambda 3727$  and  $R_{23}$  are calculated from equations 1 and 2, respectively, and then:

$$F([O II] \lambda 3727) = \frac{R_{23} \times F(H\beta)}{1.34 \times 10^{\log([O III] \lambda 5007/[O II] \lambda 3727)} + 1} \times 10^{-0.640c}. \quad (6)$$

Using the calculated flux of  $[O II] \lambda 3727$  and the values for  $R_{23}$  from equation 2, we then obtained the model value for the  $[O III] \lambda 5007$  flux:

$$F([O III] \lambda 5007) = \frac{R_{23} \times F(H\beta) - F([O II] \lambda 3727)}{1.34} \times 10^{-0.298c}. \quad (7)$$

Using the grid parameters given in Table 3, we thus created about  $12 \times 10^6$  models, each yielding 4 model flux ratios, or equivalently 5 model fluxes  $M_i$ ,  $i = 1, ..5$ , with  $H\alpha$  set to one ( $M_4 = 1$ ) as described above.

### 3.2. The best fit abundances, extinction values and ionisation parameters

For each of the 30 galaxies of our sample, combining the new H $\alpha$  and [N II]  $\lambda$  6584 measurements with the available optical CFHT measurements of LCS03 provided us with five emission lines, namely [O II]  $\lambda$  3727, H $\beta$ , [O III]  $\lambda$  5007, H $\alpha$ , and [N II]  $\lambda$  6584. These are labelled  $D_i$ ,  $i = 1, \dots, 5$ . For the comparison with the models, we assumed a conservative minimum 10% for the uncertainties  $E_i$  of the measured fluxes,  $D_i$ .

The measured [OII], H $\beta$ , [OIII], H $\alpha$ , and [NII] fluxes (i.e.,  $D_i$ ,  $i = 1, \dots, 5$ ) were then compared with the theoretical fluxes  $M_i$ ,  $i = 1, \dots, 5$  predicted for each of the  $\sim 12 \times 10^6$  models of our grid (which covers a large range of  $A_V$ ,  $q$ , and [O/H] values). In detail, the best fit models were selected to be those which minimized the  $\chi^2$  function defined as:

$$\chi^2 = \sum_{i=1}^5 \left( \frac{c \cdot M_i - D_i}{E_i} \right)^2, \quad (8)$$

where  $c$  is a flux normalization factor required to match the model fluxes  $M_i$  and the measured fluxes  $D_i$ . The normalization  $c$  is chosen so that  $\partial\chi^2/\partial c = 0$ , which gives:

$$c = \left( \sum_{i=1}^5 \frac{D_i \cdot M_i}{E_i^2} \right) / \left( \sum_{i=1}^5 \frac{M_i^2}{E_i^2} \right). \quad (9)$$

For each of the 30 galaxies, the so-derived best fit models provide the oxygen abundance [O/H], ionisation parameter  $q$ , and  $A_V$ . The best fit [O/H] abundances and  $A_V$ s which are used in the analysis described in the following sections are given in Table 4.

### 3.3. Error bars

The error bars that we report in Table 4 are the formal  $1\sigma$  confidence intervals for the projected best-fitting values, yielding oxygen abundances with a formal accuracy of typically  $\lesssim 0.1$  dex, except for few objects, where the error bars are larger because these objects are near the turn-around region or because [N II]  $\lambda$  6584 is not able to break the  $R_{23}$  degeneracy. In detail, the error bars of the oxygen abundance (or  $A_V$ ) are given by the range of oxygen abundance (or  $A_V$ , respectively) for those models with  $\chi^2$  in the range  $\chi_{min}^2 \leq \chi^2 \leq \chi_{min}^2 + 1$  (where  $\chi_{min}^2$  is the minimum  $\chi^2$  of all allowed models for a given galaxy), corresponding to a confidence level of 68.3% for one single parameter.

Figure 4 shows the  $\chi^2$  values projected onto the [O/H] axis, showing that generally only one metallicity solution is possible, and also showing the formal range of allowed models.

The horizontal (red) line in each panel corresponds to  $\chi_{min}^2 + 1$ . If only one peak (with a corresponding  $\chi_{min}^2$ ) is intersected by this line, which is the case for almost all (28/30) CFRS galaxies, then the minimum and maximum oxygen abundances given by the intersection points are used to determine the error bars of the oxygen abundance.

It should be noted that we consider a possible second solution corresponding to the second (higher) peak, only if the minimum  $\chi^2$  of the higher peak lies in the range  $\chi_{min}^2 \leq \chi^2 \leq \chi_{min}^2 + 1$ . There are two of the 30 CFRS galaxies where an alternate model is not strongly excluded ( $1 < (\chi^2 - \chi_{min}^2) < 2$ ). In these two cases we also consider the alternative oxygen abundance solutions (corresponding to the higher, less probable peak) and will indicate them as open squares wherever [O/H] is plotted. The two alternative solutions are [O/H]= $8.51_{-0.19}^{+0.19}$  for object 03.0145, and [O/H]= $8.85_{-0.04}^{+0.05}$  for object 03.9003.

It should be also noted that the shape of the  $\log R_{23}$  vs. [O/H] relation is flatter in the high metallicity region (of the high metallicity branch) than in the turn-around and low metallicity region (see Figure 5 in KD02 - rotated by 90 degrees). Therefore the lower metallicity galaxies in our sample should have larger error bars than the high metallicity galaxies, as we obtain.

In terms of absolute measurements of metallicity there are three source of uncertainties:

(a) the purely statistical measurement uncertainties propagating through to the parameter determinations. These are addressed by our  $\chi^2$  analysis. They reflect both the quality of the data and the gradients (and degeneracies) in the models. These uncertainties are presented in Table 4.

(b) Second, there are additional uncertainties arising from the methodology - e.g., averaging together the light from all of the HII regions in the galaxies to derive some kind of average [O/H]- probably at the  $\pm 0.1$  dex level (Kobulnicky et al. 1999).

(c) Uncertainties in the Kewley and Dopita models. Application of many different  $R_{23}$  calibrations to the SDSS data (Sara Ellison private communication, Ellison and Kewley 2005, submitted) indicates a range of  $\pm 0.2$  dex in the mean [O/H] at a given luminosity - with the KD02 models more or less in the middle. This latter problem is reduced by using the same analysis on all objects and focussing on differential effects with  $z$  or  $L$ , rather than estimates of the absolute metallicity.

Our philosophy is to treat all galaxies at high and low redshift in the same way and to focus on relative effects between the selected samples. Therefore, when comparing metallicities of the different samples, we think it is more appropriate to consider the uncertainty (a) described above.

### 3.4. Comparison with the oxygen abundances of LCS03

In Fig. 5 we compare the best fit [O/H] abundances derived with the new method (and based on the full set of five emission lines) with the [O/H] estimates derived from  $R_{23}$  alone assuming extinction  $A_V = 1$ , and presented in LCS03. Despite a substantial scatter, Fig. 5 shows, on average, a good agreement between the old and new [O/H] estimates. The discrepancies seen in the figure between the LCS03 and our measurements based on the KD02 method are due to the following: a) low [N II]  $\lambda$  6584/H $\alpha$  ratios for 5/30 galaxies imply that the upper branch assumption of LCS03 was incorrect for those 5 galaxies; and b) the extinction derived using the best fits of five emission lines are higher or lower compared to the  $A_V = 1$  assumed by LCS03, affecting  $R_{23}$  and thus the derived oxygen abundance. We discuss the physical basis and the implications of the agreement (and scatter) in Fig. 5 in more detail in the discussion below.

## 4. Results and Discussion: Metallicities, SFRs and dust in normal galaxies at $z \sim 1$

### 4.1. The nearby comparison sample

As in LCS03, we choose the Jansen et al. (2000, NFGS) galaxy sample as a local comparison sample. This sample was selected from the first CfA redshift catalog, and includes  $z < 0.04$  galaxies of all morphological types. The galaxies span 8 mag in luminosity and a broad range of environments. The spectra are integrated over most of the luminous parts of the galaxies and should thus be similar to the unresolved spectra of CFRS medium-redshift galaxies. From the NFGS sample of 196 objects we have extracted the 108 galaxies with measured emission fluxes for the five lines of [OII], H $\beta$ , [OIII], H $\alpha$ , and [NII].

Additionally we also use as a local comparison sample 70 galaxies from the KPNO International Spectroscopic Survey (KISS, Melbourne & Salzer 2002) which also have measured line fluxes for the five emission lines mentioned above. KISS identifies emission line galaxies candidates out to a redshift of  $z = 0.095$  by selecting objects with detectable H $\alpha$  or [O III]  $\lambda$  5007 in the low-dispersion objective-prism spectra of the survey. It should be noted that for the 70 KISS galaxies only line *ratios* are available: [O II]  $\lambda$  3727/H $\beta$  (from Melbourne & Salzer 2002), [O III]  $\lambda\lambda$  4959, 5007/H $\beta$ , [N II]  $\lambda$  6584/H $\alpha$ , and H $\alpha$ /H $\beta$  (kindly provided to us by James Melbourne). Therefore, for these 70 KISS galaxies we can calculate [O/H] using our method, but not the (dust-corrected) star formation rates from the H $\alpha$  fluxes.

## 4.2. Star formation or AGNs?

An essential step required for proceeding with the interpretation of the line emission properties of the intermediate- $z$  galaxies is to establish whether the source of gas ionisation is of stellar origin, or rather associated with AGN activity. In order to identify galaxies possibly dominated by an AGN, we can now use the  $\log([\text{O III}] \lambda 5007/\text{H}\beta)$  versus  $\log([\text{N II}] \lambda 6584/\text{H}\alpha)$  diagnostic diagram presented in Fig. 6.

AGN-dominated galaxies should appear above the solid line which represents the theoretical threshold between star forming galaxies and AGNs predicted by Kewley et al. (2001). Similarly to the nearby star forming galaxies of the combined NFGS+KISS comparison sample, it should be noted that all of the CFRS galaxies lie below the theoretical curve, indicating that in all of them the dominant source of ionisation in the gas is recent star formation.

## 4.3. $[\text{N II}] \lambda 6584/\text{H}\alpha$ as surrogate for oxygen abundance?

Pettini & Pagel (2004) derived an empirical calibration for the oxygen abundance based only on the  $[\text{N II}] \lambda 6584/\text{H}\alpha$  ratio:  $12+\log(\text{O}/\text{H}) = 8.90+0.57 \times \log([\text{N II}] \lambda 6584/\text{H}\alpha)$ . Fig. 7 shows the oxygen abundances for the 30 CFRS galaxies with 5 emission line fluxes measured versus their  $[\text{N II}] \lambda 6584/\text{H}\alpha$  ratios, compared with the Pettini & Pagel (2004) relation between oxygen abundance and the  $[\text{N II}] \lambda 6584/\text{H}\alpha$  ratio. It is obvious from this diagram that the Pettini & Pagel (2004) relation is only a very rough estimate of oxygen abundances. This is consistent with the finding of KD02 based on their Fig. 7: for  $\log([\text{N II}] \lambda 6584/\text{H}\alpha) > -0.8$  the  $[\text{NII}]/\text{H}\alpha$  metallicity relationship breaks down. Although such high  $[\text{NII}]/\text{H}\alpha$  ratios indicate an oxygen abundance on the upper branch of the  $R_{23}$  relation,  $[\text{N II}] \lambda 6584/\text{H}\alpha$  cannot be used to estimate a metallicity in this regime. At lower  $[\text{NII}]/\text{H}\alpha$  values, the  $[\text{NII}]/\text{H}\alpha$  ratio is less sensitive to metallicity and more dependent on  $R_{23}$  and ionisation parameter. Therefore,  $[\text{N II}] \lambda 6584/\text{H}\alpha$  can be used to determine the upper/lower branch of the  $R_{23}$  relation, but it is only a very crude estimate of the oxygen abundance.

## 4.4. Dust extinction, metal enrichment, and extinction-corrected SFRs

The good agreement seen in Fig. 5 between the  $[\text{O}/\text{H}]$  estimates based on  $R_{23}$  and the new more accurate estimates derived by including the  $\text{H}\alpha$  and  $[\text{N II}] \lambda 6584$  fluxes into the derivation of the gas abundances comes from two things.

First, the new NIR spectra allow us to determine the  $[\text{N II}] \lambda 6584/\text{H}\alpha$  ratios for the in-

dividual galaxies. These are expected to be  $> 0.1$  for galaxies that lie on the high-metallicity branch of the  $R_{23}$  calibration. Indeed, we find such high values of  $[\text{N II}] \lambda 6584 / \text{H}\alpha$  for most of our CFRS galaxies, confirming the assumption made in LCS03. Note however that 5/30 CFRS galaxies are on the lower branch, but near the turn around region of the  $R_{23}$  relation.

Second, the best fits to the five emission lines discussed in Section 3.2 provide a mean extinction  $A_V \sim 1$  for the CFRS galaxies. This is the same as the  $A_V = 1$  value that was assumed in LCS03 for the whole sample, establishing that most of the metal-enriched  $z \sim 1$  galaxies are indeed not heavily obscured by dust.

On the other hand, the scatter around the mean  $A_V$  value that we derive from the NIR data is large, as shown in Fig. 8. In detail, the assumed  $A_V = 1 \pm 0.5$  in LCS03 is correct for only 11 of the 30 CFRS galaxies ( $\sim 37\%$ ), is overestimated for 12 galaxies ( $\sim 40\%$ ), and is underestimated for 7 ( $\sim 23\%$  of the sample). This indicates that it is important to determine the extinction for every single galaxy in order to obtain reliable gas oxygen abundances in high redshift galaxies.

The availability of the individual extinction values  $A_V$  for our sample galaxies allows us to derive extinction-corrected SFRs from the  $\text{H}\alpha$  fluxes. For each CFRS galaxy, we calculated the SFR using the Kennicutt (1998) conversion of  $\text{H}\alpha$  luminosity into  $\dot{M}$ :  $\text{SFR}(M_{\odot}\text{yr}^{-1}) = 7.9 \times 10^{-42} L(\text{H}\alpha) \text{ergs/s}$ . The resulting extinction-corrected SFRs of the 30 CFRS galaxies range between 1 and  $70 M_{\odot}\text{yr}^{-1}$ . Fig. 8 shows the SFR vs. extinction for the 30 CFRS galaxies (filled squares) and local NFGS galaxies (filled circles) indicating that CFRS galaxies have extinction properties broadly similar to nearby galaxies with similar SFRs and luminosities.

We did not find strong correlations between any pairs of galaxy properties, from absolute  $B$  magnitude  $M_{B,AB}$ , oxygen abundance  $[\text{O}/\text{H}]$ , restframe  $(U - V)_{AB,0}$  color, extinction  $A_V$ , extinction-corrected SFR, and ionisation parameter  $q$ . This was established by performing a Principal Component Analysis using these quantities as Eigenvectors. It should be noted, however, that the range of measured parameters within the sample and the number of galaxies are both quite small.

The only strong correlation found by this analysis was between extinction  $A_V$  and the extinction-corrected SFR, as seen also in Fig. 8. Obviously, such a relation could have been produced by an error in  $A_V$ : if the  $A_V$  estimates were randomized, given the narrow range in  $\text{H}\beta$  fluxes in our sample, we would still get a distribution with a mean relation parallel to the direction of the error vector (dotted line in Fig. 8). We do not think that this is the case.

The CFRS sample was selected by LCS03 to have an equivalent width  $EW(\text{H}\beta) > 8\text{\AA}$ ,

and the sample of our 30 CFRS galaxies has a selection against objects below the dotted line. However, there is no selection against galaxies with low extinction and high star formation rates, which would appear in the upper left corner of Fig. 8, but which are apparently missing.

The star formation rates *not* corrected for extinction for the 30 CFRS galaxies (open squares in Fig. 8, derived from  $H\alpha$  luminosities not corrected for extinction) show no correlation with  $A_V$ . Therefore, if galaxies are lacking measurements of the Balmer lines required to determine the extinction, assuming a similar  $A_V$  for galaxies with similar (*not* extinction-corrected)  $H\alpha$  luminosities would lead to wrong estimates of the real SFRs. This suggests that it is important to determine the extinction for every single galaxy in order to obtain reliable measurements for the SFRs of high redshift galaxies.

#### 4.5. The metallicity-luminosity (mass) relation

A metallicity-luminosity relation is observed in the local universe (e.g., Melbourne & Salzer 2002; Lamareille et al. 2004; Tremonti et al. 2004), in the sense that more luminous galaxies tend to be more metal-rich. Fig. 9, an update of Fig. 10 in LCS03, shows  $M_{B,AB}$  vs.  $[O/H]$  for the local NFGS and KISS galaxies and the fits to the respective data, which result in a metallicity-luminosity relation of similar slope and zero-point for both samples, which we use as local comparison. The 30 CFRS galaxies with measured  $H\alpha$  are plotted as filled squares in this diagram. Moreover, as an update of Fig. 17 in LCS03, Fig. 10 shows  $M_{J,AB}$  (a surrogate for the stellar mass) vs.  $[O/H]$  for the 20 galaxies with available K photometry.

In both diagrams the higher metallicity CFRS galaxies overlap with the region of the diagram occupied by local galaxies of similar luminosity (mass). The lower metallicity CFRS galaxies ( $[O/H] < 8.6$ ) are more luminous (massive) than local galaxies with similar  $[O/H]$ , and more metal-poor than local galaxies with similar absolute luminosities. A similar trend is seen in Fig. 11 for the SFR- $[O/H]$  relation: the CFRS galaxies with higher metallicities overlap with the region of the diagram occupied by local galaxies with similar SFRs, while the lower metallicity CFRS galaxies ( $[O/H] < 8.6$ ) have higher SFRs than local galaxies with similar  $[O/H]$ , and are more metal-poor than local galaxies with similar SFRs.

Comparing the average value of  $[O/H]$  for the 30 CFRS galaxies to the average value of  $[O/H]$  of NFGS and KISS local galaxies with similar luminosities in Fig. 9, we find that the average change in metallicity is about 0.3 dex between galaxies at  $z \sim 0.7$  and  $z \sim 0$ . It is not hard to get a change by a factor of two between  $z \sim 0.7$  and  $z \sim 0$ . For instance, Pégase2 models (Fioc & Rocca-Volmerange 1999) discussed by Maier et al. (2004) can get a track as shown by the dashed curve and symbols in Fig. 9, according to which the metallicity

of the intermediate redshift CFRS galaxies may increase by a factor of about 2 by  $z \sim 0$ . In this scenario the lower metallicity CFRS galaxies may fade by 0.5-0.9 mag by  $z \sim 0$ , due to decreasing levels of star formation, and migrate in the metallicity-luminosity and metallicity-SFR diagram (Figs. 9, 10, and 11) to the region occupied by local galaxies with lower luminosities and higher [O/H].

Assuming a uniform  $A_V = 1$  LCS03 found  $\sim 25\%$  of the galaxies in their CFRS sample to have lower metallicities, i.e.  $[\text{O}/\text{H}] < 8.6$ , but pointed out that if  $A_V = 0$  for all galaxies in their sample the fraction of galaxies with  $[\text{O}/\text{H}] < 8.6$  dropped to 5%. Our new data, which allow the determination of extinction for each individual galaxy, confirm a high average  $A_V$ , and, not surprisingly, a high fraction, actually about one third (but in a smaller sample than those used by LCS03), of lower metallicity galaxies (see Fig. 9).

Kobulnicky et al. (2003) apparently did not find the medium redshift  $M_B \sim -21$  galaxies with lower metallicities  $[\text{O}/\text{H}] < 8.6$  in their sample. This could be explained by the fact that Kobulnicky et al. (2003) did not correct the fluxes of their  $0.26 < z < 0.82$  galaxy sample for extinction. Correcting for reddening would increase  $R_{23}$  and move objects with apparently high metallicity to lower metallicity. Also, if not all the objects were on the upper branch, as assumed by Kobulnicky et al. (2003) based on  $[\text{N II}] \lambda 6584/\text{H}\alpha$  measured for 9 ( $z < 0.4$ ) galaxies of their 64 objects, might result in a lower metallicity for some of the galaxies.

Our new measurements of  $\text{H}\alpha$  and  $[\text{N II}] \lambda 6584$  confirm the low metallicity population of galaxies at  $M_B \sim -21$  found by LCS03. It is unlikely (see also LCS03, and Maier et al. 2004) that these low metallicity galaxies are the progenitors of today’s metal-poor dwarf galaxies ( $M_B \sim -17$ ), because they would need to fade too much compared with the observational results of the evolution of the luminosities of galaxies at  $0 < z < 1.5$ : e.g., Wolf et al. (2003) found a maximum fading of 2 mag between  $z \sim 1.2$  and  $z \sim 0$ . Moreover, chemical evolution models generally produce rather “oblique” than “horizontal” tracks: the evolution in the metallicity-luminosity diagram would be from bottom right to upper left, with galaxies evolving from low metallicity and high luminosities towards higher metallicities and fainter luminosities, as shown by the model in Fig. 9.

A more detailed discussion of the metallicity-luminosity relation at  $0 < z < 3$  including our additional measurements of oxygen abundances of galaxies at  $z \sim 1.4$  and comparison to theoretical chemical evolution models will be given in a separate paper (Maier et al. 2005, Paper IV in our series).

## 5. Conclusions

The metallicity of the star forming gas has been measured for 30 CFRS galaxies with  $0.47 < z < 0.92$  using optical CFHT and near-infrared VLT-ISAAC and Keck-NIRSPEC spectroscopy. Using the measurements of five emission lines it was possible to determine the extinction, oxygen abundances and extinction corrected star forming rates for these 30 luminous ( $M_{B,AB} \lesssim -19.5$ ) galaxies. The sample was extracted from the 66 CFRS galaxies for which LCS03 obtained estimates of oxygen abundances based on 3 emission line fluxes ([O II]  $\lambda$  3727, H $\beta$ , and [O III]  $\lambda$  5007). The additional H $\alpha$  and [N II]  $\lambda$  6584 obtained by the near-infrared spectroscopy lead us to the following conclusions:

1. The source of gas ionisation in the 30 CFRS galaxies is not associated with AGN activity, as derived from the  $\log([\text{O III}] \lambda 5007/\text{H}\beta)$  versus  $\log([\text{N II}] \lambda 6584/\text{H}\alpha)$  diagnostic diagram.

2. The mean extinction  $A_V \sim 1$  for the 30 CFRS galaxies is the same as the uniform  $A_V = 1$  value assumed by LCS03. However, the large scatter  $0 < A_V < 3$  indicates the importance of the determination of the extinction for every single galaxy, to obtain reliable oxygen abundances and star forming rates at high redshift.

3. Most galaxies have  $[\text{N II}] \lambda 6584/\text{H}\alpha > 0.1$  confirming the assumption made in LCS03 that most CFRS galaxies lie on the high-metallicity branch of the  $R_{23}$  calibration. However, a minority of them (5/30) lie on the lower branch, although near the turn-around region.

4. 20 of the 30 CFRS galaxies at  $0.47 < z < 0.92$  have the higher metallicities ( $[\text{O}/\text{H}] > 8.6$ ) found locally in galaxies of similar luminosities. However, one third of the CFRS galaxies have substantially lower metallicities than local galaxies with similar luminosities and star formation rates. This is at the upper band of the range found by LCS03 for the fraction of lower metallicities objects, and is due to the fact that we can account for the variety of reddening when computing the oxygen abundances. We also find that the average change in metallicity is about 0.3 dex between the CFRS galaxies and local galaxies of similar luminosities.

5. The evolution of the lower metallicities CFRS galaxies will be probably oblique in the metallicity-luminosity diagram: these galaxies will probably increase their metallicities by about 0.3 dex and decrease their luminosities by about 0.5-0.9 mag, evolving into the region occupied by today's  $z \sim 0$  galaxies. Therefore they are unlikely be the progenitors of the metal-poor dwarf galaxies seen today.

We would like to thank Lisa Kewley for pursuing with us the problem of truncated coefficients in the KD02 paper, and for kindly sending us the coefficients with more decimal places which accurately reproduce the KD02 theoretical models. We also want to thank James Melbourne for kindly sending us  $[\text{N II}] \lambda 6584/\text{H}\alpha$  and  $\text{H}\alpha/\text{H}\beta$  for KISS galaxies. We are also grateful the anonymous referee for his/her suggestions which have improved the paper. CM acknowledges support from the Swiss National Science Foundation.

## REFERENCES

- Brocklehurst M. 1971 MNRAS, 153, 471
- Carollo, C. M. & Lilly, S. J. 2001, ApJ, 548, 153, CL01
- Fioc, M. & Rocca-Volmerange, B., 1999, astro-ph/9912179
- Hammer, F., Gruel, N., Thuan, T. X., Flores, H., and Infante, L., 2001, ApJ, 550, 570
- Hippelein, H., Maier, C., Meisenheimer, K. et al. 2003, A&A, 402, 65
- Horne K. 1986, PASP, 98, 609
- Izotov, Y. I., Thuan, T. X. & Lipovetsky, V. A. 1994, ApJ, 435, 647
- Jansen, R. A., Fabricant, D., Franx, M. et al, 2000, ApJS, 126, 331
- Kennicutt, R. C., Jr. 1998, ARA&A, 36, 189
- Kewley, L.J., Heisler, C.A., Dopita, M.A.& Lumsden, S. 2001, ApJS, 132, 37
- Kewley, L.J. & Dopita, M.A., 2002, ApJSS, 142, 35, KD02
- Kobulnicky, H. A., Kennicutt. R.C., and Pizgano, J. L., 1999, ApJ, 514, 544
- Kobulnicky, H. A., Wilmer C. N. A., Weiner, B. J. et al. 2003, ApJ, 599, 1006
- Kobulnicky, H. A. & Kewley, L.J. 2004, ApJ 617, 240
- Lamareille, F., Mouhcine, M., Contini, T., Lewis, I. & Maddox, S., 2004, MNRAS, 350, 396
- Lilly, S.J, Carollo, C.M. & Stockton, A. 2003, ApJ, 597, 730, LCS03
- Maier, C., Meisenheimer, K., Hippelein, H., 2004, A&A, 418, 475
- Maier, C. et al., 2005, in preparation
- Mehlert, D., Noll, S., Appenzeller, I. et al. 2002, A&A, 393, 809
- Melbourne, J. & Salzer, J. J. 2002, AJ, 123, 2302
- Osterbrock, D.E. 1989, Astrophysics of Gaseous Nebulae and Active Galactic Nuclei (Mill Valley: University Science Books)
- Pagel, B. E. J., Edmunds, M. G., Blackwell, D. E. et al. 1979, MNRAS, 189, 95

- Pettini, M., Rix, S.A., Steidel, C.C. et al. 2002, *Ap&SS*, 281, 461
- Pettini, M. 2003, *astro-ph/0303272*
- Pettini, M. & Pagel, B.E.J. *MNRAS*, 2004, 348, 59
- Salzer, J. J., Lee, J.C., Melbourne, J. et al., 2005, *ApJ*, 624, 661
- Seaton, M. J. *MNRAS* 1979, 187, 73
- Shapley, A., Erb, D. K., Pettini, M. et al. 2004, *ApJ*, 612, 108
- Tremonti, C. A., Heckman, T. M., Kauffmann, G. et al. 2004, *ApJ*, 613, 898
- van Dokkum, P. G. 2001, *PASP*, 113, 1420
- Whitford, A. E., 1958, *AJ*, 63, 201
- Wolf, C., Meisenheimer, K., Rix, H.-W. et al 2003, *A&A*, 401, 73

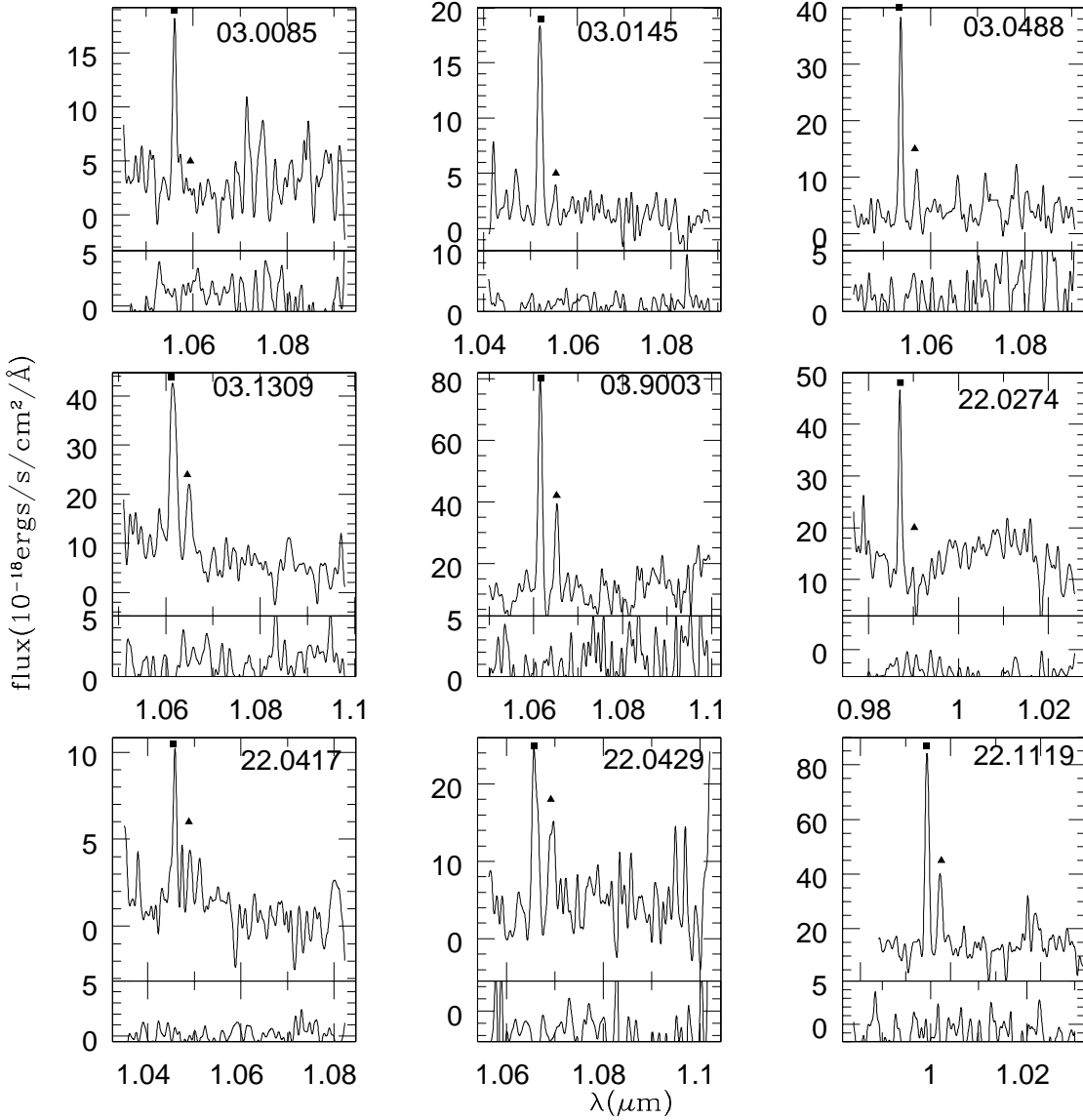


Fig. 1.— ISAAC spectra using the SZ filter for the 5th grating order in order to get H $\alpha$  and [N II]  $\lambda$ 6584 for galaxies at  $0.5 < z < 0.65$ . The spectra are smoothed with a Gaussian filter, as described in the text. In each figure, the filled square and the filled triangle show the position of H $\alpha$  and [N II]  $\lambda$ 6584, respectively. Almost all galaxies show a [N II]  $\lambda$ 6584/H $\alpha$  ratio greater than 0.1, as expected for galaxies that lie on the high-metallicity branch of the  $R_{23}$  calibration.

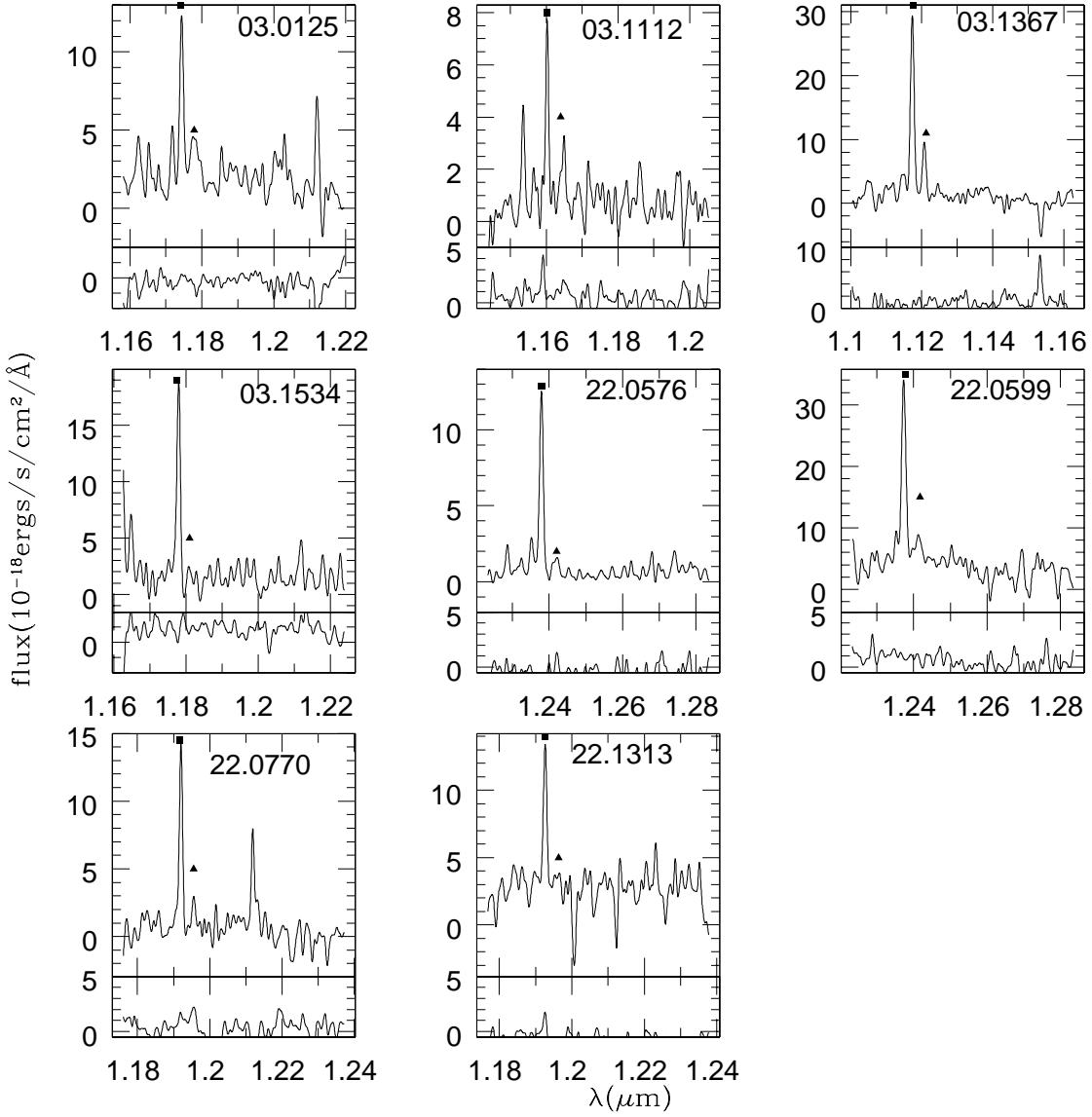


Fig. 2.— Like Fig. 1, but using the J filter for the 4th grating order in order to get  $\text{H}\alpha$  and  $[\text{N II}] \lambda 6584$  for galaxies at  $0.7 < z < 0.92$ . Almost all galaxies show a  $[\text{N II}] \lambda 6584/\text{H}\alpha$  ratio greater than 0.1, as expected for galaxies that lie on the high-metallicity branch of the  $R_{23}$  calibration.

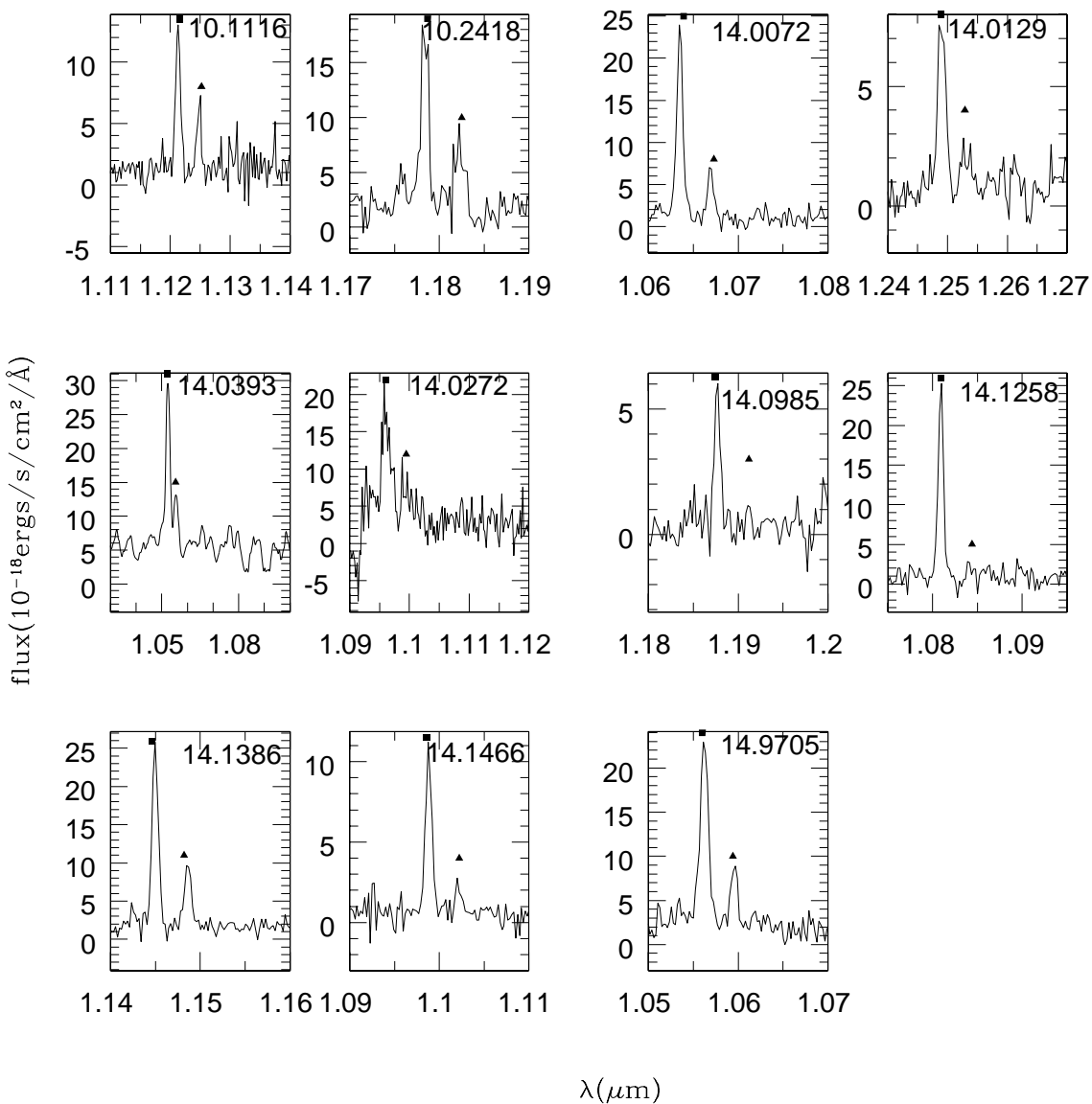


Fig. 3.— NIRSPEC spectra using Keck. In each figure, the filled square and the filled triangle show the position of  $\text{H}\alpha$  and  $[\text{N II}] \lambda 6584$ , respectively. Almost all galaxies show a  $[\text{N II}] \lambda 6584/\text{H}\alpha$  ratio greater than 0.1, as expected for galaxies that lie on the high-metallicity branch of the  $R_{23}$  calibration.

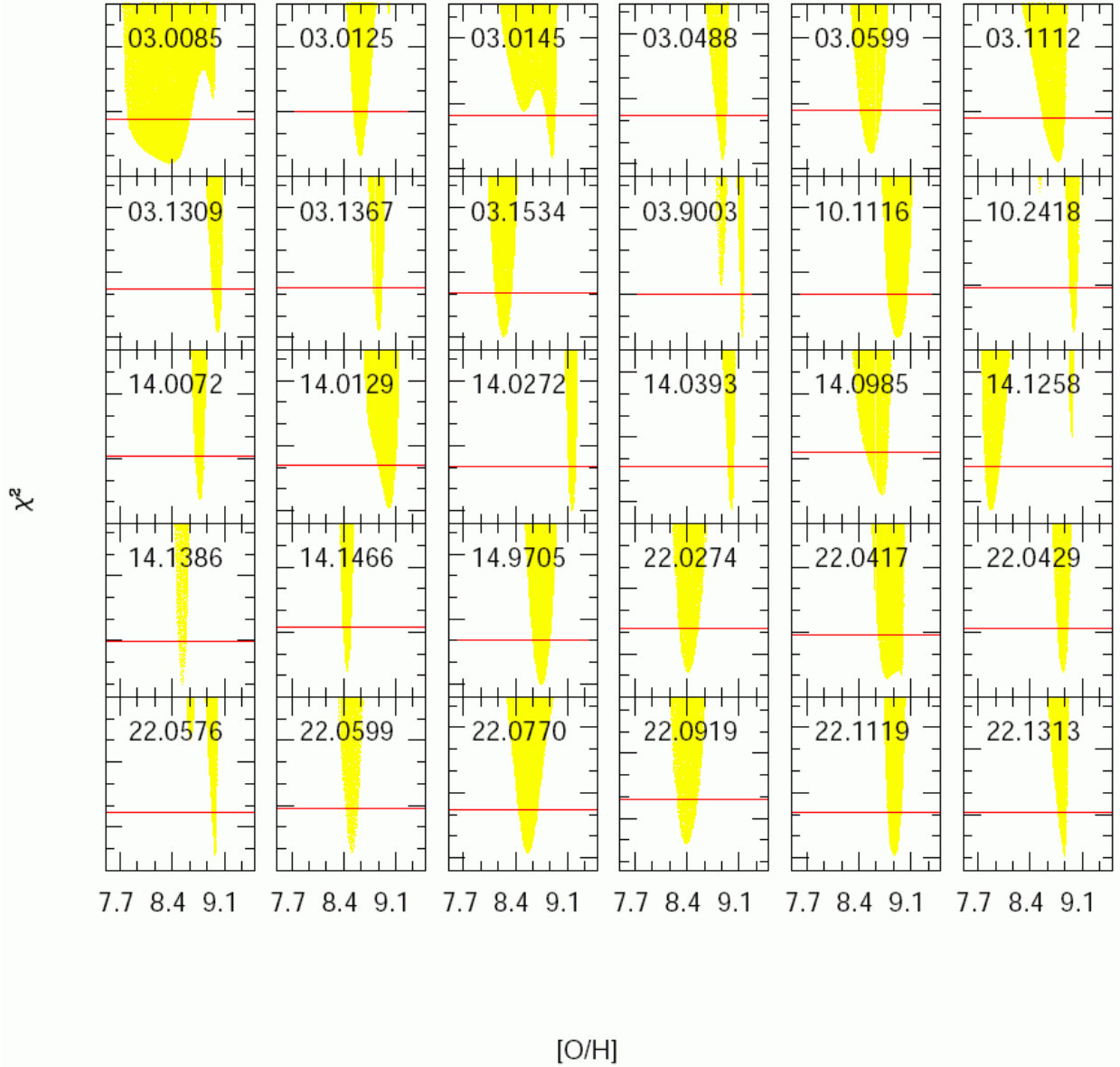


Fig. 4.—  $\chi^2$  values projected onto the [O/H] axis for the most probable models for each of the 30 CFRS galaxies. The horizontal (red) line in each panel corresponds to  $\chi_{min}^2 + 1$ , where  $\chi_{min}^2$  is the minimum  $\chi^2$  of all allowed models for a given galaxy. If only one peak (with a corresponding  $\chi_{min}^2$ ) is intersected by this line, which is the case for almost all (28/30) CFRS galaxies, then the minimum and maximum oxygen abundances given by the intersection points are used to determine the error bars of the oxygen abundance.

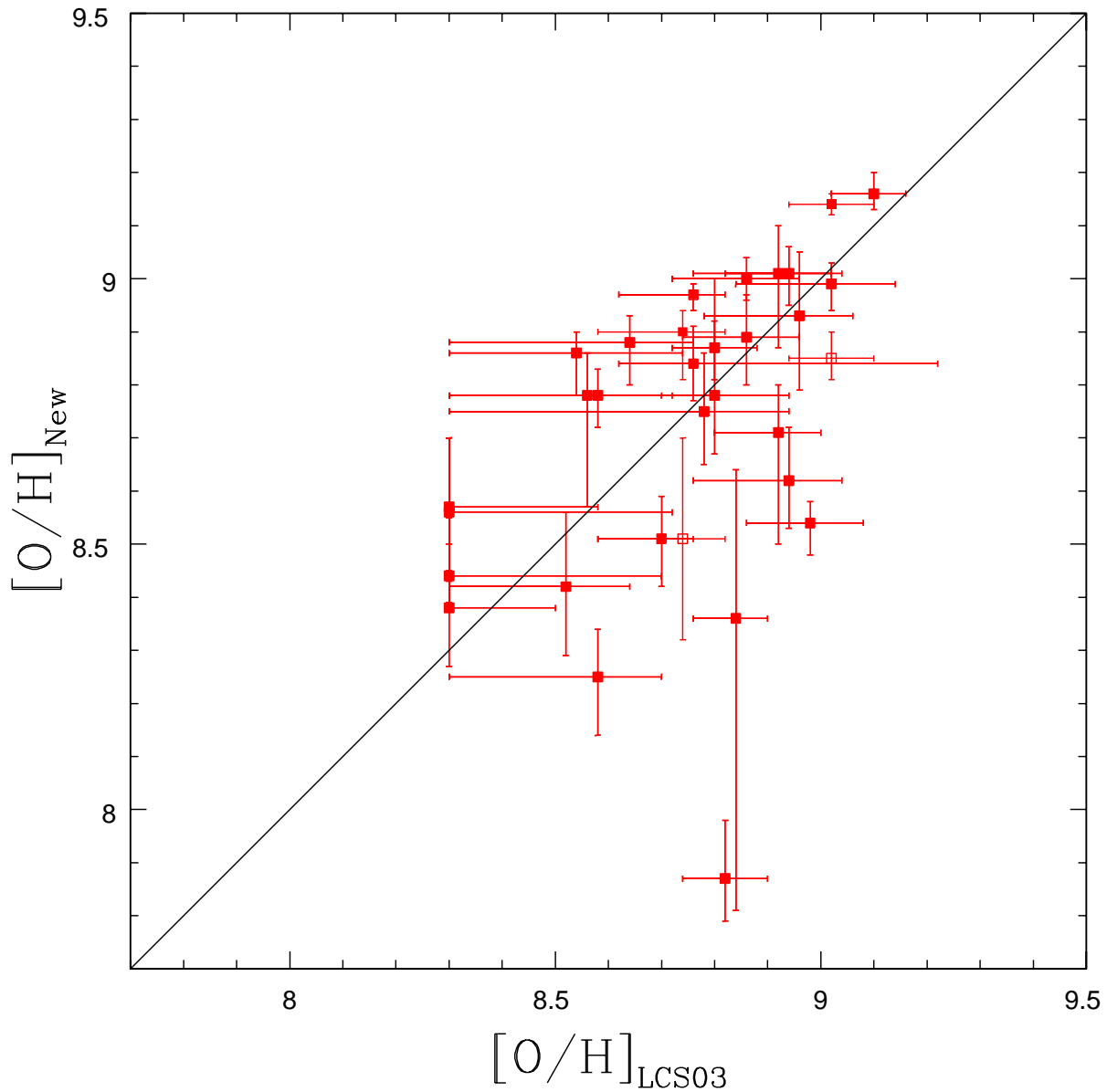


Fig. 5.— Comparison of the best fit  $[O/H]$  abundances derived with the new method for 30 CFRS galaxies (and based on the full set of five emission lines) with the  $[O/H]$  estimates derived from  $R_{23}$  and presented in LCS03. The two open squares are the alternative (but less probable) oxygen abundance solutions for two CFRS galaxies, as discussed in Section 3.3. In the Sections 3.4 and 4.4 we discuss the physical basis and the implications of the agreement and scatter seen in the figure.

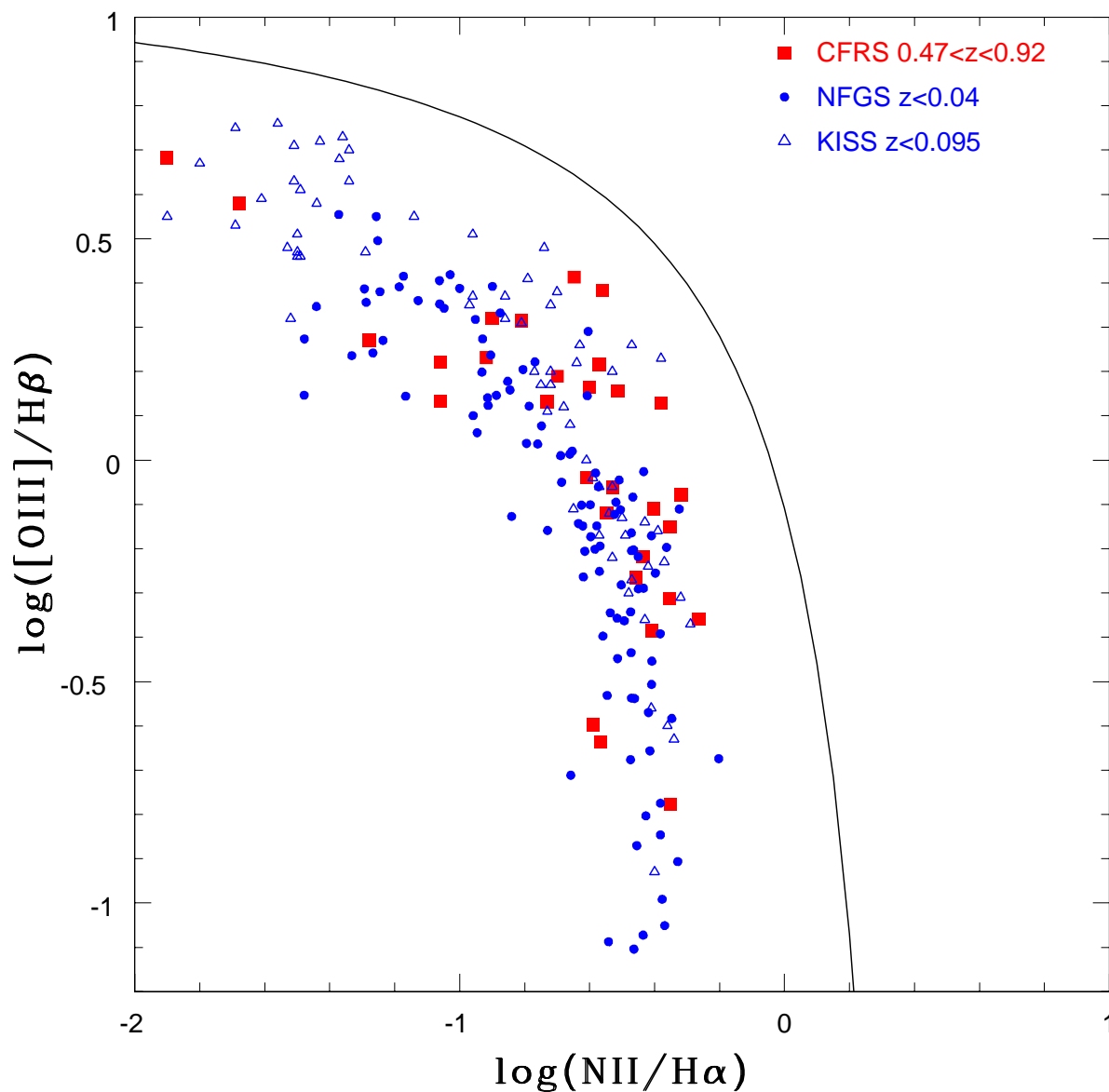


Fig. 6.— Diagnostic diagram for the 30 CFRS galaxies at  $0.47 < z < 0.92$  (filled squares), 108 local NFGS galaxies (filled circles), and 70 KISS galaxies (open triangles). The solid line shows the theoretical curve of Kewley et al. (2001) above which galaxies are dominated by an AGN. Similarly to the nearby star forming galaxies of the combined NFGS+KISS comparison sample, all of the CFRS galaxies lie below the theoretical curve, indicating that in all of them the dominant source of ionisation in the gas is recent star formation.

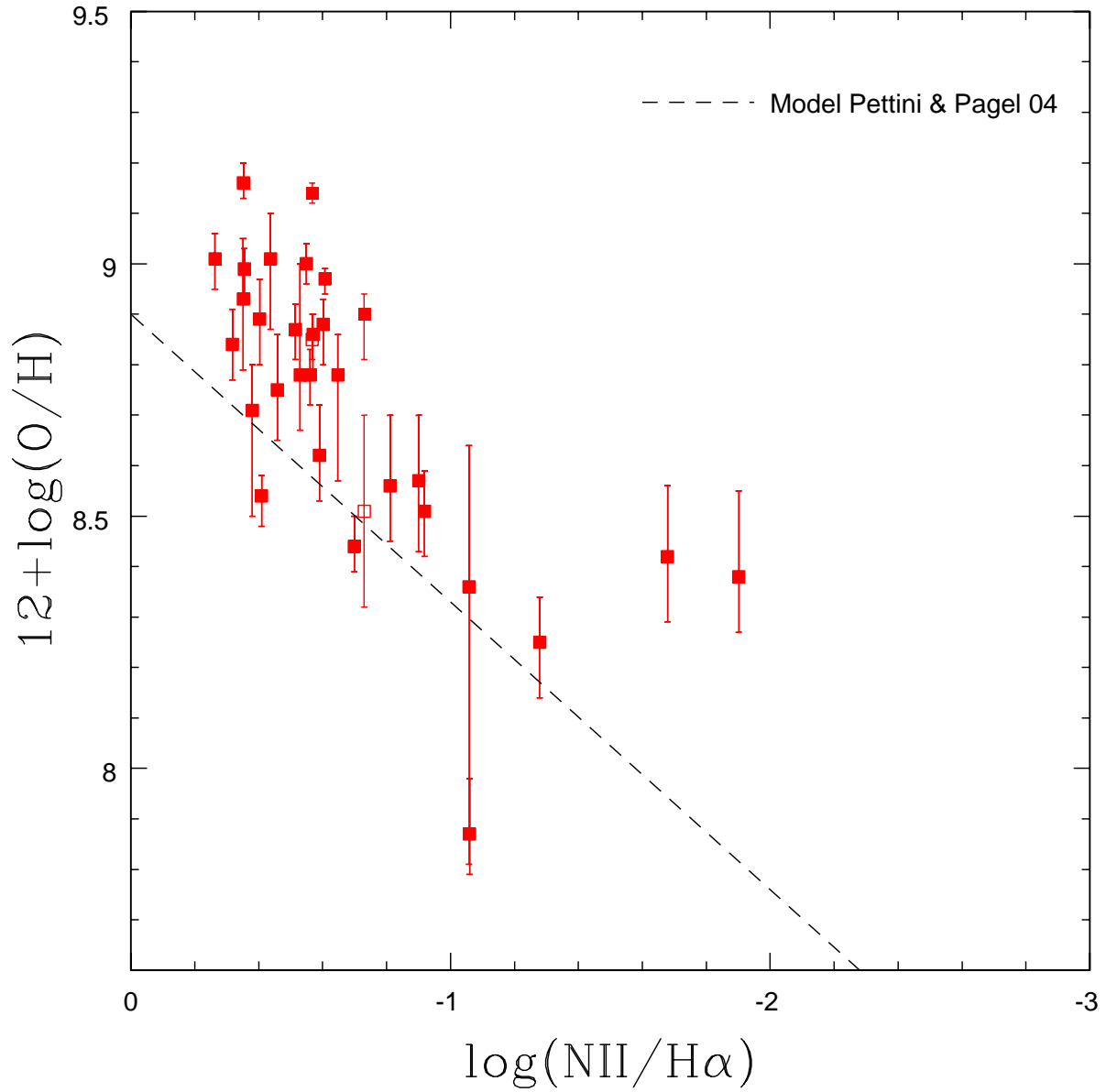


Fig. 7.—  $[O/H]$  based on 5 measured emission lines versus  $[NII] \lambda 6584/H\alpha$  for the 30 CFRS galaxies compared to the Pettini & Pagel (2004) relation between  $[NII] \lambda 6584/H\alpha$  and metallicity (dotted line). As discussed in Section 4.3,  $[NII] \lambda 6584/H\alpha$  can be used to determine the upper/lower branch of the  $R_{23}$  relation, but it is only a very crude estimate of the oxygen abundance.

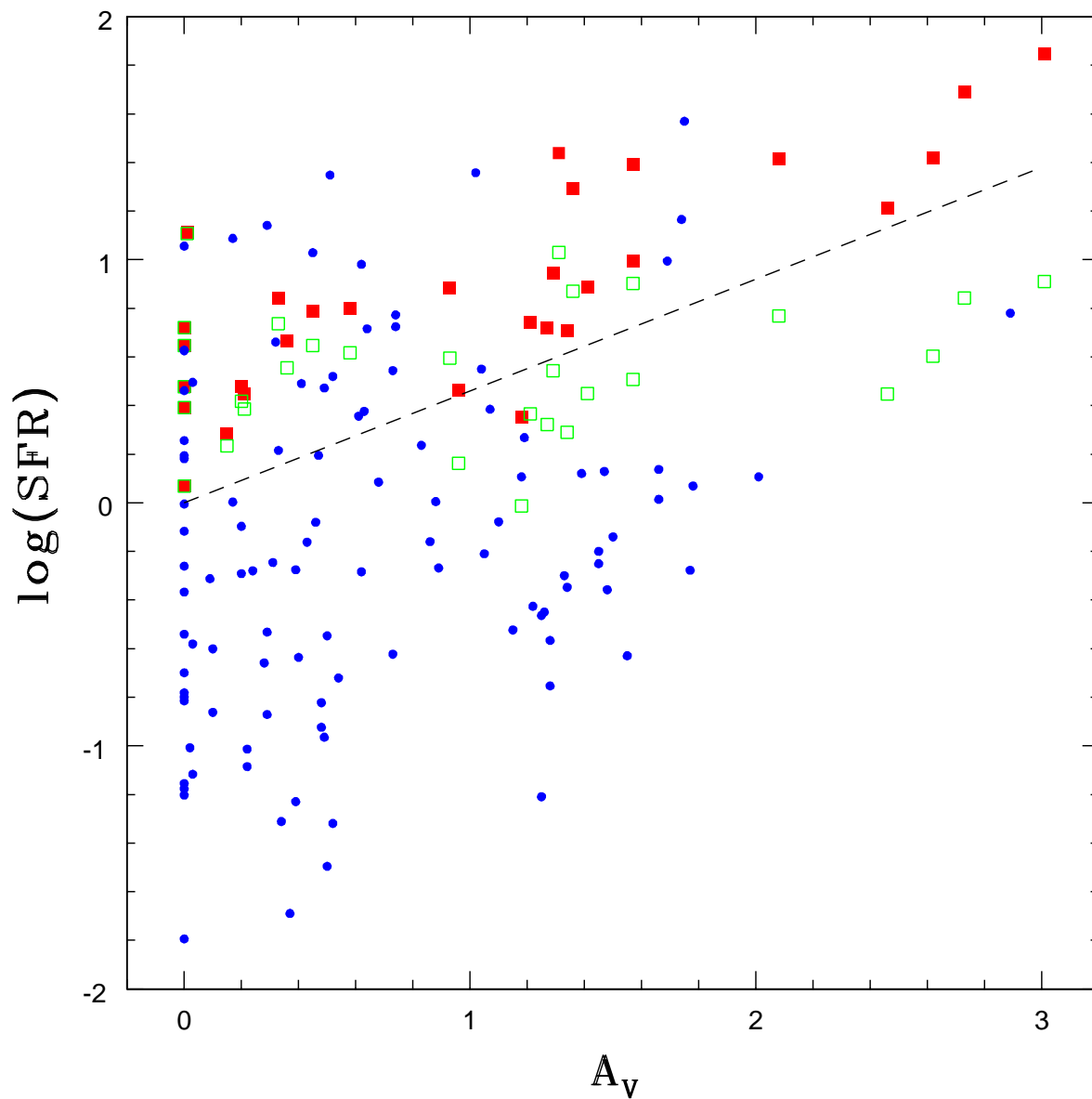


Fig. 8.— Extinction corrected  $\log(\text{SFR})$  vs.  $A_V$  for the 30 CFRS (filled squares) and NFGS galaxies (filled circles). The star formation rates *not* corrected for extinction for the 30 CFRS galaxies (open squares) show no correlation with  $A_V$ . Therefore, if galaxies are lacking measurements of *both*  $H\alpha$  and  $H\beta$  to determine the extinction, one *cannot* use a similar  $A_V$  value for galaxies with similar *not* extinction-corrected  $H\alpha$  luminosities (SFRs). It is important to determine the extinction for every single galaxy in order to obtain reliable measurements for the SFRs.

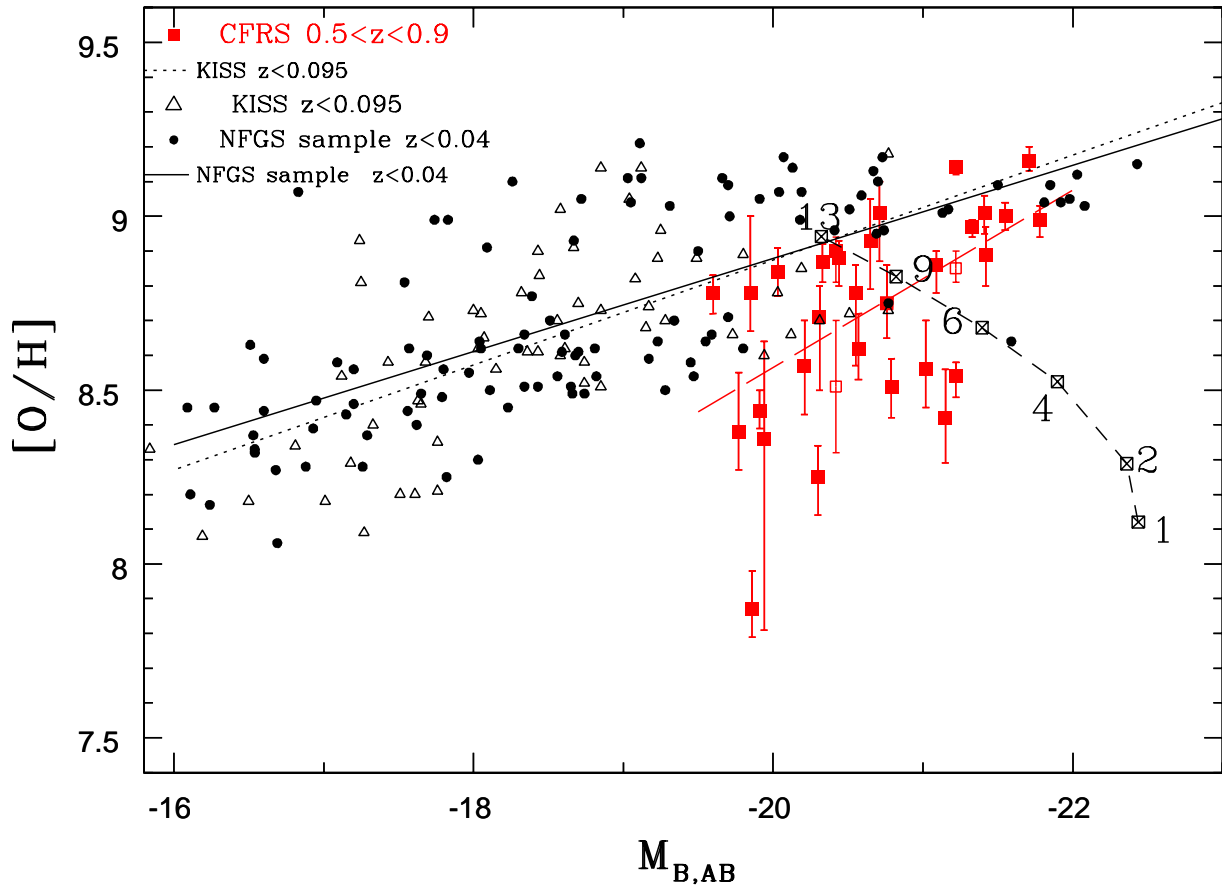


Fig. 9.— Oxygen abundance versus  $M_{B,AB}$  for the 30 CFRS galaxies (filled squares), NFGS local galaxies (filled circles), and local KISS galaxies (open triangles). The dashed line shows the resulting metallicity-luminosity relation of the 30 CFRS galaxies. The two open squares are the alternative (but less probable) oxygen abundance solutions for two CFRS galaxies, as discussed in Section 3.3. The lower metallicity CFRS galaxies are consistent with evolving into NFGS and KISS galaxies with slightly (0.5-0.9 mag) lower luminosities and higher metallicities (a factor of  $\sim 2$ ), as shown by an example scenario discussed by Maier et al. (2004); note that the symbols along the track indicate the age of the model galaxy.

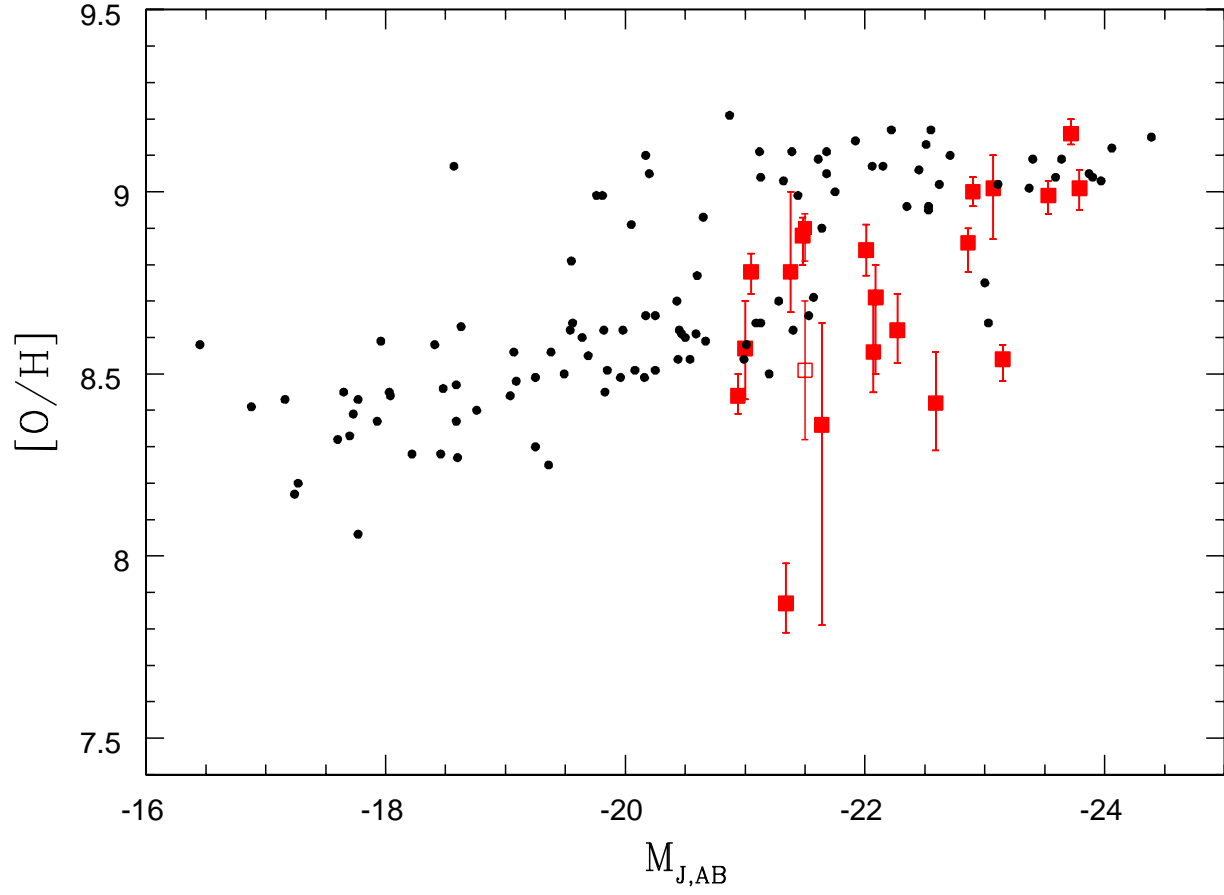


Fig. 10.— Oxygen abundance versus  $M_{J,AB}$  for the 20 CFRS galaxies with available K photometry (filled squares), and NFGS local galaxies (filled circles). The lower metallicity CFRS galaxies are consistent with evolving into NFGS and KISS galaxies with slightly lower luminosities and higher metallicities (see also Fig. 9).

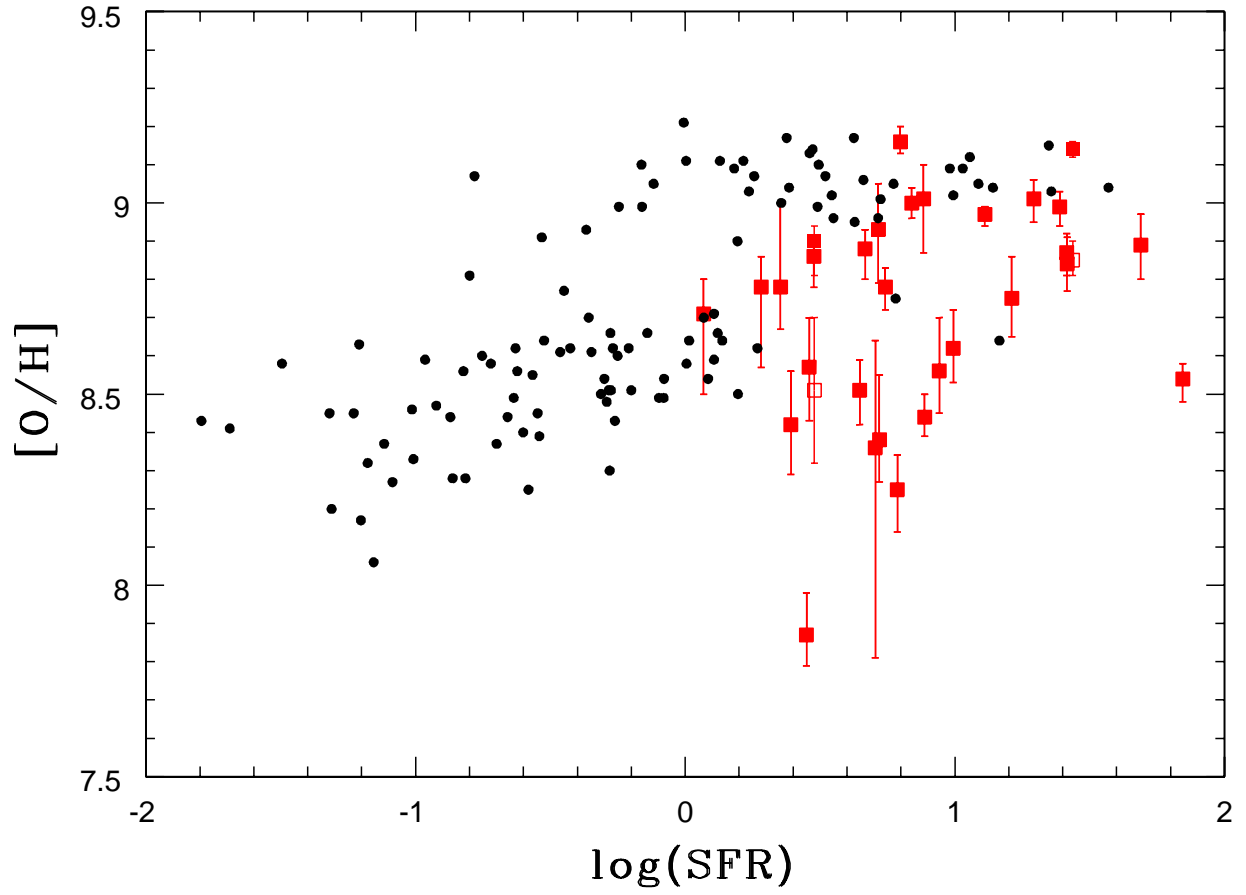


Fig. 11.— Oxygen abundance  $[O/H]$  vs.  $\log(SFR)$  for the 30 CFRS galaxies (filled squares), and for the local NFGS galaxies (filled circles). The lower metallicity CFRS galaxies are consistent with evolving into NFGS and KISS galaxies with slightly lower luminosities and higher metallicities, due to decreasing levels of star formation (see also Fig. 9).

Table 1. The 30  $0.47 < z < 0.92$  CFRS galaxies

Obj	redshift	U	B	V	R	I	Z	K	$\log(r_{0.5})^a M_{B,AB}$	$M_{J,AB}$	[O II] $\lambda 3727^{b,c}$	H $\beta^{b,c}$	[O III] $\lambda 5007^{b,c}$	H $\alpha^b$	[N II] $\lambda 6584^b EW_{H\alpha}(\text{\AA})$		
03.0085	0.609	23.51	23.39	22.91	22.17	21.80	21.62	21.32	*	-19.94	-21.64	8.80±0.33	4.57 ±2.0	7.70±0.20	16 ±2	1.4 ± 1.2	60
03.0125	0.789	23.72	23.45	23.19	22.48	21.84	21.67	20.87	0.61	-20.57	-22.27	10.10±0.26	4.85 ±1.4	1.30±1.2	14 ±2	3.6 ± 0.8	80
03.0145	0.603	22.55	22.48	22.22	21.58	21.32	21.30	21.10	0.74	-20.42	-21.50	17.70±0.66	6.21 ±0.54	8.80±0.40	22 ±3	4.1 ± 1.3	100
03.0488	0.605	22.87	22.69	22.61	21.90	21.64	21.57	21.31	0.32	-20.44	-21.48	25.50±0.66	9.06 ±1.03	13.80±0.33	30± 3	7.5± 1.5	60
03.0599	0.479	22.59	22.44	21.94	21.36	21.18	21.11	21.25	0.68	-20.21	-21.00	20.50±0.66	4.17 ±0.78	9.00± 0.40	21.3±1.0	2.68 ± 2.0	130
03.1112	0.768	23.60	23.61	23.46	23.03	22.45	22.29	*	*	-20.55	*	8.50±0.33	2.62 ±1.1	7.00±0.33	8 ±2	1.8 ± 0.7	100
03.1309	0.617	22.24	22.24	21.87	21.19	20.99	20.87	19.32	0.95	-21.41	-23.79	25.70±0.33	13.00±2.00	5.90±0.40	59 ±5	32.2 ± 3.2	70
03.1367	0.703	22.76	22.42	22.44	21.74	21.37	21.29	*	*	-20.33	*	10.50±0.40	5.82 ±0.42	9.20±0.40	34 ±3	10.4 ± 0.7	150
03.1534	0.794	23.17	23.19	23.16	22.73	22.24	22.26	*	*	-20.30	*	17.00±0.33	5.73 ±0.35	10.80±0.26	19± 2	1 ± 0.4	75
03.9003	0.618	22.77	22.41	22.00	21.20	20.83	20.63	*	*	-21.22	*	12.00±0.20	10.10±1.78	2.60 ±0.40	85± 8	23 ± 3	70
10.1116	0.709	*	*	*	*	*	*	*	*	-20.65	*	7.1 ±0.30	2.66 ±1.0	2.00±1.5	11.9±1	5.3 ±0.7	95
10.2418	0.796	*	*	*	*	*	*	20.14	*	-21.78	-23.53	7.05 ±0.88	5.53 ±0.55	3.00 ±2.0	34 ±3	15 ± 1	105
14.0072	0.621	23.73	23.63	23.32	22.76	22.42	22.45	21.30	*	-19.60	-21.05	11.20 ±0.26	4.22 ±0.22	10.80±0.26	18.2±1.5	5.0 ± 0.7	160
14.0129	0.903	24.57	24.28	23.82	23.37	22.48	22.30	20.63	*	-20.71	-23.07	5.00 ±0.20	3.04 ±0.9	2.0 ±2.0	12.3±1.0	4.5 ± 0.5	200
14.0272	0.670	22.58	22.29	21.75	21.11	20.47	20.27	19.28	*	-21.71	-23.72	6.90 ±0.26	7.65 ±1.17	1.60±0.40	27 ±3	12 ± 2	60
14.0393	0.603	22.18	21.93	21.47	20.83	20.46	20.34	19.56	0.75	-21.55	-22.90	30±0.35	13.38±1.52	10.19±0.57	46 ±3	13 ± 4	80
14.0985	0.809	24.47	24.38	23.85	23.50	22.53	22.29	21.42	0.44	-20.31	-22.09	8 ±1	2.83 ±0.7	3.80±0.40	4.8 ±0.5	2 ± 1.0	105
14.1258	0.647	24.12	23.95	23.64	22.94	22.64	22.46	21.58	0.26	-19.86	-21.34	9.2 ±0.5	5.63 ±0.22	7.7 ±0.7	17.2±1.0	1.5 ± 1.0	190
14.1386	0.744	23.40	23.11	22.57	21.94	21.38	21.11	19.84	*	-21.22	-23.15	9.32 ±0.18	6.07 ±0.78	2.79±0.29	41 ±4	16 ± 2	100
14.1466	0.674	23.87	23.75	23.34	22.68	22.38	22.24	21.33	0.45	-19.91	-20.94	11.80 ±0.66	3.21 ±0.27	5.20±0.26	18 ±1	3.6 ± 0.6	150
14.9705	0.609	23.23	22.79	21.99	21.64	21.30	20.97	*	*	-20.76	*	8.8 ±1.0	3.38 ±0.45	2.0 ±0.7	23 ±1.5	8 ± 2	85
22.0274	0.504	22.19	21.91	21.05	20.70	20.40	20.35	19.90	*	-21.15	-22.59	32.00±3.0	11.85±1.03	45±4.0	32 ±5	0.67 ±1.24	50
22.0417	0.593	24.47	23.90	23.31	22.37	21.97	21.84	21.22	*	-19.85	-21.38	6.90±0.26	2.86 ±1.4	2.60±0.26	8.5 ±1	2.51 ±0.49	50
22.0429	0.624	24.77	24.02	23.46	22.45	21.89	21.67	20.49	*	-20.03	-22.01	10.20±0.33	3.98 ±0.46	3.60±0.33	31 ±5	14.90±2.38	100
22.0576	0.886	23.58	23.35	22.89	22.61	21.98	21.75	*	0.35	-21.33	*	31.00±0.33	12.22±0.41	11.70±1.32	42 ±4	10.37±1.21	105
22.0599	0.887	23.28	22.99	22.57	22.22	21.68	21.53	*	0.04	-20.79	*	25.00±0.33	11.09±0.19	18.90±0.66	14.5±1.5	1.75 ±0.40	200
22.0770	0.816	23.80	23.67	23.22	22.75	22.04	21.96	21.71	*	-21.02	-22.07	10.50±0.26	2.69 ±1.3	4.00±0.33	14 ±2	2.16 ±0.69	120
22.0919	0.472	22.41	22.51	21.92	21.91	21.33	21.50	*	*	-19.77	*	51.00±0.66	29.63±0.75	143.00±0.66	79.8±4.0	1.0 ± 2.0	230
22.1119	0.514	22.21	21.89	21.20	20.40	20.03	19.80	*	*	-21.42	*	20.80±0.46	11.55±2.10	10.00±5.0	86 ±5	34 ±3	100
22.1313	0.817	23.49	23.44	23.34	22.65	21.90	21.77	21.16	0.73	-21.09	-22.86	13.60±0.40	4.89 ±0.9	8.20±0.40	12 ±2	3.23 ±0.73	50

<sup>a</sup>half-light radius  $r_{0.5}$

<sup>b</sup>Fluxes in  $10^{-17} \text{ergs s}^{-1} \text{cm}^{-2}$

<sup>c</sup>from the CFHT optical observations presented in LCS03

Table 2: Spectroscopic follow-up with VLT and Keck

#	Filter	$t_{exp}$ (s)	Night	Seeing	Telluric Standard
VLT-ISAAC					
03.0085	SZ	2400	2003 Nov 18/19	1".1	Hip031190
03.0145	SZ	2400	2003 Nov 18/19	1".2	Hip031190
03.0488	SZ	1800	2004 Oct 08/09	1".0	Hip026098
03.1309	SZ	2400	2003 Dec 03/04	1".1	Hip031190
03.9003	SZ	1800	2004 Sep 22/23	1".2	Hip023551
22.0274	SZ	1200	2002 Oct 11/12	1".2	Hip109332
22.0417	SZ	4800	2002 Oct 17/18	0".7	Hip109332
22.0429	SZ	2400	2002 Oct 10/11	1".3	Hip109332
22.1119	SZ	1800	2002 Oct 09/10	1".2	Hip109332
03.0125	J	2400	2003 Nov 18/19	0".7	Hip031190
03.1112	J	2400	2003 Dec 03/04	0".8	Hip031190
03.1367	J	2400	2003 Dec 03/04	0".8	Hip031190
03.1534	J	2400	2004 Oct 08/09	1".0	Hip026098
22.0576	J	1200	2002 Oct 11/12	1".2	Hip109332
22.0599	J	1200	2002 Oct 11/12	1".2	Hip109332
22.0770	J	3600	2002 Oct 10/11	0".9	Hip100556
22.1313	J	2400	2002 Oct 06/07	0".7	Hip000183
Keck-NIRSPEC <sup>a</sup>					
10.1116	NS2	2400	2004 Mar 29/30	0".7	HD89239
10.2418	NS2	2400	2004 Mar 30/31	0".5	86 UMa
14.0072	NS1	2400	2004 Mar 30/31	0".5	86 UMa
14.0129	NS3	2400	2004 Mar 30/31	0".7	HD129653
14.0272	NS2	2400	2004 Mar 29/30	0".7	HD89239
14.0393	NS1	2400	2000 June 14/15	0".7	HD89239
14.0985	NS2	2400	2004 Mar 29/30	0".7	HD129653
14.1258	NS1	2400	2004 Mar 30/31	0".6	86 UMa
14.1386	NS2	2400	2004 Mar 29/30	0".7	HD129653
14.1466	NS2	2400	2004 Mar 29/30	0".7	HD129653
14.9705	NS1	2400	2004 Mar 30/31	0".6	HD129653

<sup>a</sup>NIRSPEC uses a set of order-sorting filters to cover the range from 0.95 to 2.6 microns; these are called “NIRSPEC-1”, “NIRSPEC-2”, etc., and abbreviated in the table as “NS1” (0.947 – 1.121 $\mu$ m), “NS2” (1.089 – 1.293 $\mu$ m), and “NS3” (1.143 – 1.375 $\mu$ m).

Table 3: The model grid used to calculate  $A_V, q$ , and  $[O/H]$

Parameter	Range
$A_V$ (extinction parameter)	$0 < A_V < 3.01$ in 302 steps
$q$ (ionisation parameter)	$5 \cdot 10^6 \text{cm s}^{-1} < q < 300 \cdot 10^6 \text{cm s}^{-1}$ in 201 steps
$O/H$ (oxygen abundance)	$7.6 < O/H < 9.4$ in 201 steps

Table 4: Derived quantities for the 30 CFRS galaxies

#	$z$	H $\alpha$ /H $\beta$	[NII]/H $\alpha$	$A_V^a$	SFR	[O/H] <sup>a</sup>
03.0085	0.609	3.50 $\pm$ 1.59	0.09 $\pm$ 0.08	1.34 <sup>+0.40</sup> <sub>-1.34</sub>	5.08 <sup>+2.53</sup> <sub>-3.37</sub>	8.36 <sup>+0.28</sup> <sub>-0.55</sub>
03.0125	0.789	2.89 $\pm$ 0.93	0.26 $\pm$ 0.07	1.57 <sup>+0.23</sup> <sub>-0.25</sub>	9.86 <sup>+3.42</sup> <sub>-2.79</sub>	8.62 <sup>+0.10</sup> <sub>-0.09</sub>
03.0145	0.603	3.54 $\pm$ 0.57	0.19 $\pm$ 0.06	0.20 <sup>+1.34</sup> <sub>-0.20</sub>	3.02 <sup>+5.92</sup> <sub>-0.76</sub>	8.90 <sup>+0.04</sup> <sub>-0.09</sub>
03.0488	0.605	3.31 $\pm$ 0.50	0.25 $\pm$ 0.06	0.36 <sup>+0.49</sup> <sub>-0.36</sub>	4.65 <sup>+2.61</sup> <sub>-1.41</sub>	8.88 <sup>+0.05</sup> <sub>-0.08</sub>
03.0599	0.479	5.11 $\pm$ 0.99	0.13 $\pm$ 0.09	0.96 <sup>+0.23</sup> <sub>-0.25</sub>	2.89 <sup>+0.68</sup> <sub>-0.59</sub>	8.57 <sup>+0.13</sup> <sub>-0.14</sub>
03.1112	0.768	3.05 $\pm$ 1.49	0.22 $\pm$ 0.10	0.15 <sup>+0.68</sup> <sub>-0.15</sub>	1.91 <sup>+1.97</sup> <sub>-0.62</sub>	8.78 <sup>+0.08</sup> <sub>-0.21</sub>
03.1309	0.617	4.54 $\pm$ 0.80	0.55 $\pm$ 0.07	1.36 <sup>+0.49</sup> <sub>-0.43</sub>	19.59 <sup>+10.58</sup> <sub>-6.41</sub>	9.01 <sup>+0.05</sup> <sub>-0.06</sub>
03.1367	0.703	5.84 $\pm$ 0.67	0.31 $\pm$ 0.03	2.08 <sup>+0.38</sup> <sub>-0.31</sub>	25.99 <sup>+11.12</sup> <sub>-7.00</sub>	8.87 <sup>+0.05</sup> <sub>-0.06</sub>
03.1534	0.794	3.32 $\pm$ 0.40	0.05 $\pm$ 0.02	0.45 <sup>+0.26</sup> <sub>-0.33</sub>	6.12 <sup>+2.03</sup> <sub>-1.80</sub>	8.25 <sup>+0.09</sup> <sub>-0.11</sub>
03.9003	0.618	8.42 $\pm$ 1.68	0.27 $\pm$ 0.04	1.31 <sup>+0.31</sup> <sub>-0.28</sub>	27.36 <sup>+10.00</sup> <sub>-7.07</sub>	9.14 <sup>+0.02</sup> <sub>-0.02</sub>
10.1116	0.709	4.47 $\pm$ 1.72	0.45 $\pm$ 0.07	1.27 <sup>+0.61</sup> <sub>-0.94</sub>	5.21 <sup>+3.52</sup> <sub>-2.77</sub>	8.93 <sup>+0.12</sup> <sub>-0.14</sub>
10.2418	0.796	6.15 $\pm$ 0.82	0.44 $\pm$ 0.05	1.57 <sup>+0.40</sup> <sub>-0.33</sub>	24.48 <sup>+10.98</sup> <sub>-6.85</sub>	8.99 <sup>+0.04</sup> <sub>-0.05</sub>
14.0072	0.621	4.31 $\pm$ 0.42	0.27 $\pm$ 0.04	1.21 <sup>+0.29</sup> <sub>-0.28</sub>	5.52 <sup>+1.83</sup> <sub>-1.37</sub>	8.78 <sup>+0.05</sup> <sub>-0.06</sub>
14.0129	0.903	4.05 $\pm$ 1.24	0.37 $\pm$ 0.05	0.93 <sup>+1.11</sup> <sub>-0.76</sub>	7.65 <sup>+10.64</sup> <sub>-3.57</sub>	9.01 <sup>+0.09</sup> <sub>-0.14</sub>
14.0272	0.670	3.53 $\pm$ 0.67	0.44 $\pm$ 0.09	0.58 <sup>+0.47</sup> <sub>-0.46</sub>	6.28 <sup>+3.48</sup> <sub>-2.26</sub>	9.16 <sup>+0.04</sup> <sub>-0.03</sub>
14.0393	0.603	3.44 $\pm$ 0.45	0.28 $\pm$ 0.09	0.33 <sup>+0.44</sup> <sub>-0.33</sub>	6.92 <sup>+3.18</sup> <sub>-1.81</sub>	9.00 <sup>+0.04</sup> <sub>-0.04</sub>
14.0985	0.809	1.70 $\pm$ 0.46	0.42 $\pm$ 0.21	0.00 <sup>+0.17</sup> <sub>-0.00</sub>	1.17 <sup>+0.29</sup> <sub>-0.12</sub>	8.71 <sup>+0.09</sup> <sub>-0.21</sub>
14.1258	0.647	3.06 $\pm$ 0.21	0.09 $\pm$ 0.06	0.21 <sup>+0.45</sup> <sub>-0.21</sub>	2.82 <sup>+1.30</sup> <sub>-0.53</sub>	7.87 <sup>+0.11</sup> <sub>-0.08</sub>
14.1386	0.744	6.75 $\pm$ 1.09	0.39 $\pm$ 0.06	3.01 <sup>+0.03</sup> <sub>-0.08</sub>	70.02 <sup>+8.50</sup> <sub>-10.34</sub>	8.54 <sup>+0.04</sup> <sub>-0.06</sub>
14.1466	0.674	5.61 $\pm$ 0.57	0.20 $\pm$ 0.04	1.41 <sup>+0.22</sup> <sub>-0.21</sub>	7.73 <sup>+1.82</sup> <sub>-1.45</sub>	8.44 <sup>+0.06</sup> <sub>-0.05</sub>
14.9705	0.609	6.80 $\pm$ 1.01	0.35 $\pm$ 0.09	2.46 <sup>+0.26</sup> <sub>-0.32</sub>	16.26 <sup>+4.60</sup> <sub>-4.17</sub>	8.75 <sup>+0.11</sup> <sub>-0.10</sub>
22.0274	0.504	2.70 $\pm$ 0.48	0.02 $\pm$ 0.04	0.00 <sup>+0.16</sup> <sub>-0.00</sub>	2.47 <sup>+0.73</sup> <sub>-0.39</sub>	8.42 <sup>+0.14</sup> <sub>-0.13</sub>
22.0417	0.593	2.97 $\pm$ 1.50	0.30 $\pm$ 0.07	1.18 <sup>+0.37</sup> <sub>-1.18</sub>	2.26 <sup>+1.03</sup> <sub>-1.40</sub>	8.78 <sup>+0.22</sup> <sub>-0.11</sub>
22.0429	0.624	7.79 $\pm$ 1.55	0.48 $\pm$ 0.11	2.62 <sup>+0.34</sup> <sub>-0.40</sub>	26.06 <sup>+12.53</sup> <sub>-9.64</sub>	8.84 <sup>+0.07</sup> <sub>-0.07</sub>
22.0576	0.886	3.44 $\pm$ 0.35	0.25 $\pm$ 0.04	0.01 <sup>+0.30</sup> <sub>-0.01</sub>	12.91 <sup>+4.61</sup> <sub>-1.31</sub>	8.97 <sup>+0.02</sup> <sub>-0.03</sub>
22.0599	0.887	1.31 $\pm$ 0.14	0.12 $\pm$ 0.03	0.00 <sup>+0.05</sup> <sub>-0.00</sub>	4.44 <sup>+0.64</sup> <sub>-0.46</sub>	8.51 <sup>+0.08</sup> <sub>-0.09</sub>
22.0770	0.816	5.20 $\pm$ 2.62	0.15 $\pm$ 0.05	1.29 <sup>+0.27</sup> <sub>-0.31</sub>	8.77 <sup>+3.39</sup> <sub>-2.75</sub>	8.56 <sup>+0.14</sup> <sub>-0.11</sub>
22.0919	0.472	2.69 $\pm$ 0.15	0.01 $\pm$ 0.03	0.00 <sup>+0.15</sup> <sub>-0.00</sub>	5.26 <sup>+0.89</sup> <sub>-0.26</sub>	8.38 <sup>+0.17</sup> <sub>-0.11</sub>
22.1119	0.514	7.45 $\pm$ 1.42	0.40 $\pm$ 0.04	2.73 <sup>+0.30</sup> <sub>-0.59</sub>	48.92 <sup>+15.23</sup> <sub>-18.70</sub>	8.89 <sup>+0.08</sup> <sub>-0.09</sub>
22.1313	0.817	2.45 $\pm$ 0.61	0.27 $\pm$ 0.08	0.00 <sup>+0.44</sup> <sub>-0.00</sub>	3.00 <sup>+1.79</sup> <sub>-0.50</sub>	8.86 <sup>+0.04</sup> <sub>-0.08</sub>

<sup>a</sup>The quoted uncertainties are the purely statistical measurement uncertainties propagating through to parameter determinations. These are addressed by our  $\chi^2$  analysis. They reflect both the quality of the data and the gradients (and degeneracies) in the KD02 models. For more details see Section 3.3.